Extended Data Fig. 1: Single-cell transcriptomic characterization and annotation of PBMCs.

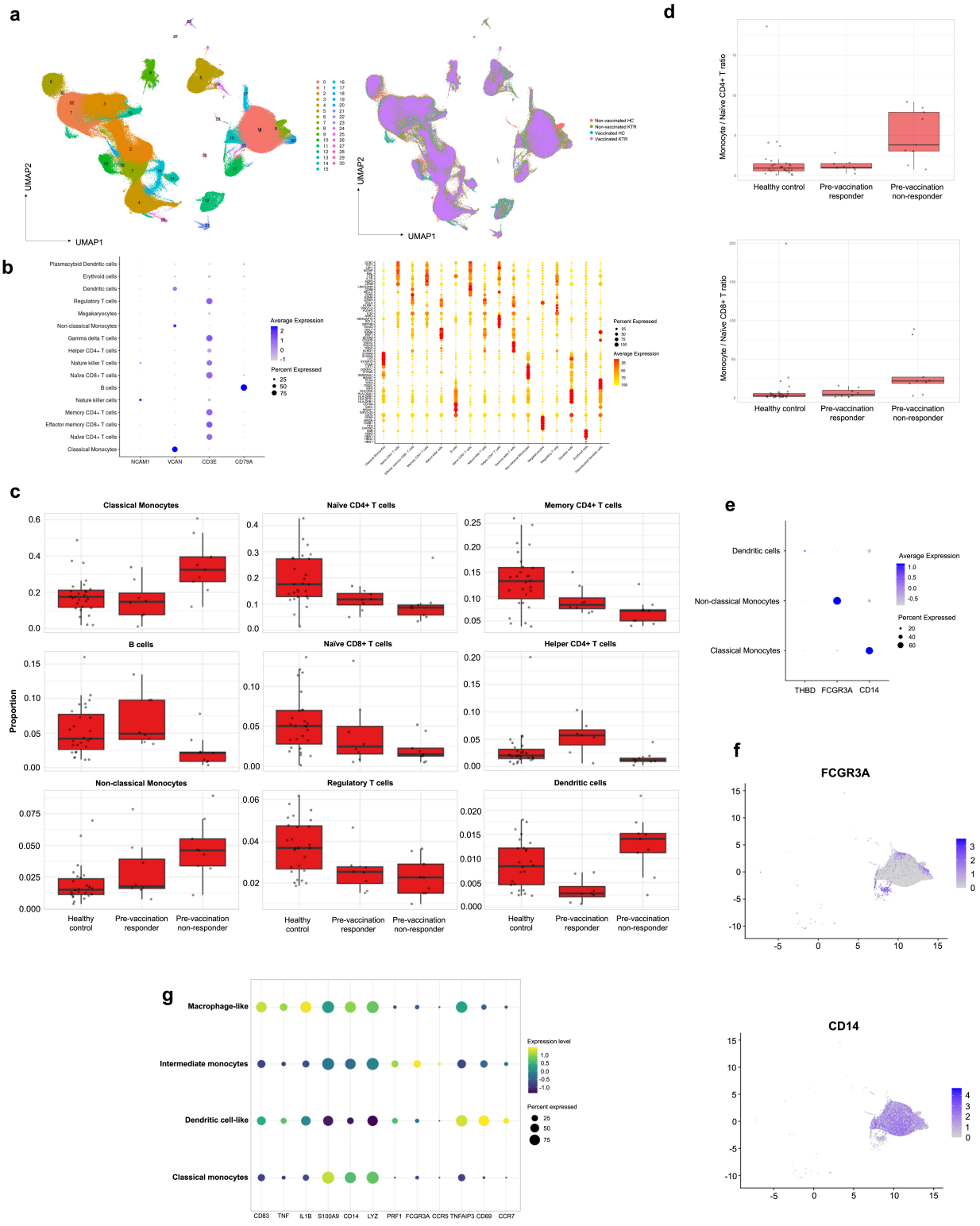

a, Left panel: UMAP projection of PBMCs colored by clusters. Right panel: UMAP projection of PBMCs colored by experimental group (HC: Healthy Control, KTR: Kidney Transplant Recipient). **b,** Left panel: Dot plot showing the expression of canonical marker genes used to define major immune cell populations. Dot size represents the proportion of cells expressing the gene, and color indicates average expression level. Right panel: Dot plot showing scaled expression of selected immune-related genes across annotated cell types. **c,** Proportion of major immune cell types showing significant differences among healthy controls (HC), responders (R), and non-responders (NR). Cell type proportions were calculated from single-cell transcriptomic profiles and compared across groups using the Kruskal–Wallis test with false discovery rate (FDR) correction (FDR < 0.05). Red boxes represent the interquartile range, black lines indicate the median, and whiskers denote the 1.5× interquartile range. **d,** Ratios of monocytes to naïve $CD4^+$ T cells (top) and monocytes to naïve $CD8^+$ T cells (bottom) across clinical groups. Each point represents an individual subject from healthy controls (HC), pre-vaccination responders (Pre-vac R), and pre-vaccination non-responders (Pre-vac NR). Ratios were calculated from the relative proportions of the indicated immune cell types in peripheral blood single-cell transcriptomic data. Boxes indicate the interquartile range (IQR) with the median line; whiskers extend to 1.5 × IQR. Statistical significance was assessed using the Kruskal–Wallis test with Benjamini–Hochberg correction for multiple comparisons. **e,** Dot plot highlighting the expression of *FCGR3A* and *CD14* across identified monocyte subclusters. **f,** Feature plots of *FCGR3A* (top) and *CD14* (bottom) expression on the UMAP, used to distinguish classical and non-classical monocytes. **g,** Dot plot showing the expression of marker genes across identified monocyte sub-phenotypes.

Extended Data Fig. 2: Mitochondrial and glycolytic rewiring reveal immune readiness defects in non-responder monocytes.

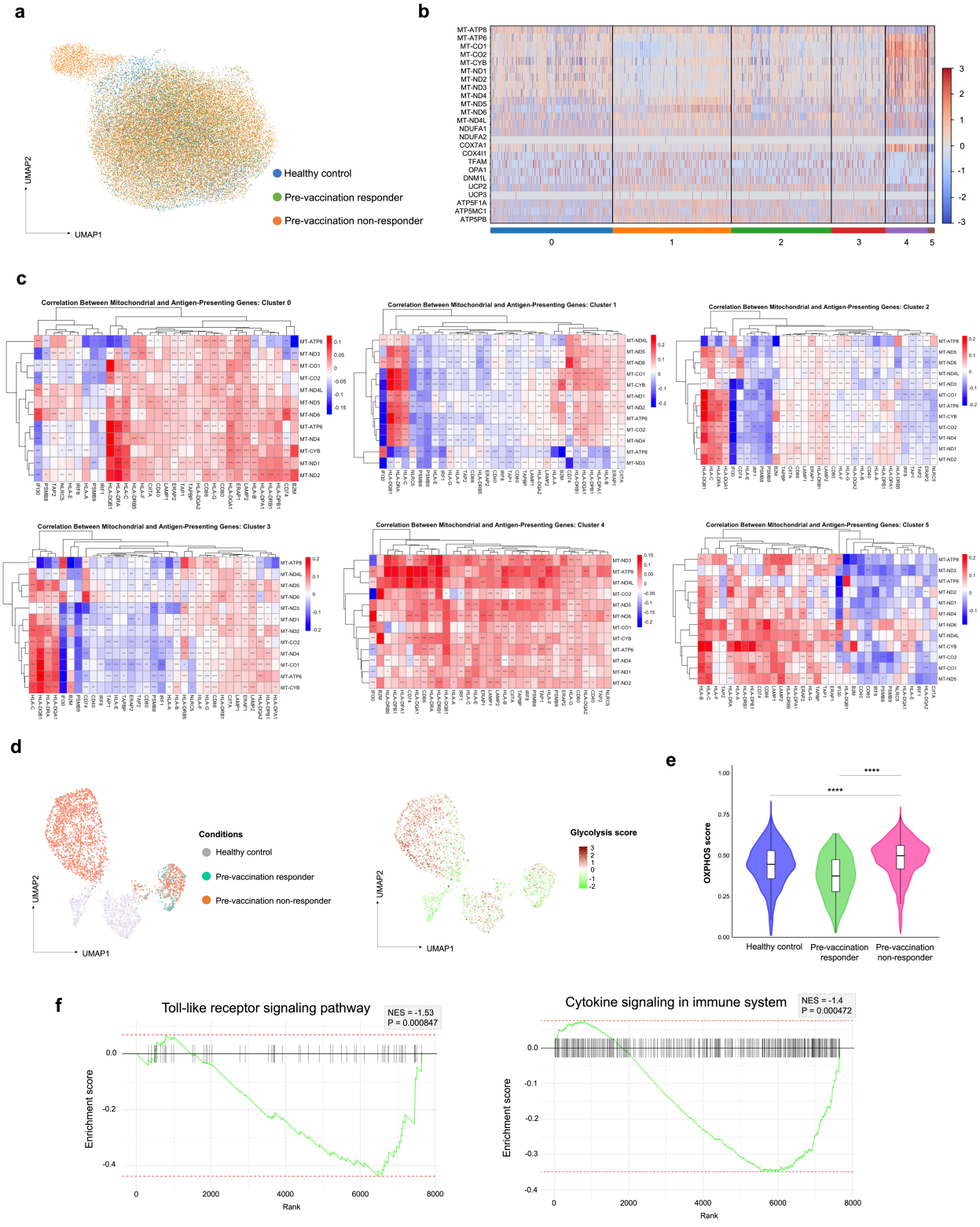

a, UMAP projection of monocytes colored by condition (Healthy control, Pre-vaccination responder, Pre-vaccination non-responder). **b,** Heatmap showing scaled expression of mitochondrial-encoded genes, nuclear-encoded mitochondrial genes, and genes involved in mitochondrial dynamics and energy metabolism. Cells are grouped into six clusters. Colors indicate relative expression levels (red, high; blue, low). **c,** Correlation heatmaps showing gene–gene correlations between mitochondrial-encoded genes and antigen-presenting genes within each monocyte subcluster. Color represents Pearson correlation coefficients. **d,** UMAP projections showing monocytes colored by condition (left) and glycolysis signature score (right). **e,** Violin plot showing OXPHOS score across conditions. **f,** GSEA enrichment plots showing significant downregulation of the toll-like receptor signaling pathway (left) and cytokine signaling in immune system (right) in non-responder monocytes compared to responders. Running enrichment score (green line), ranked gene list (black vertical lines), and normalized enrichment score (NES) with nominal *P*-value are indicated in each panel.

Extended Data Fig. 3: Dysregulated late-stage monocyte activation in metabolically rewired NR monocytes.

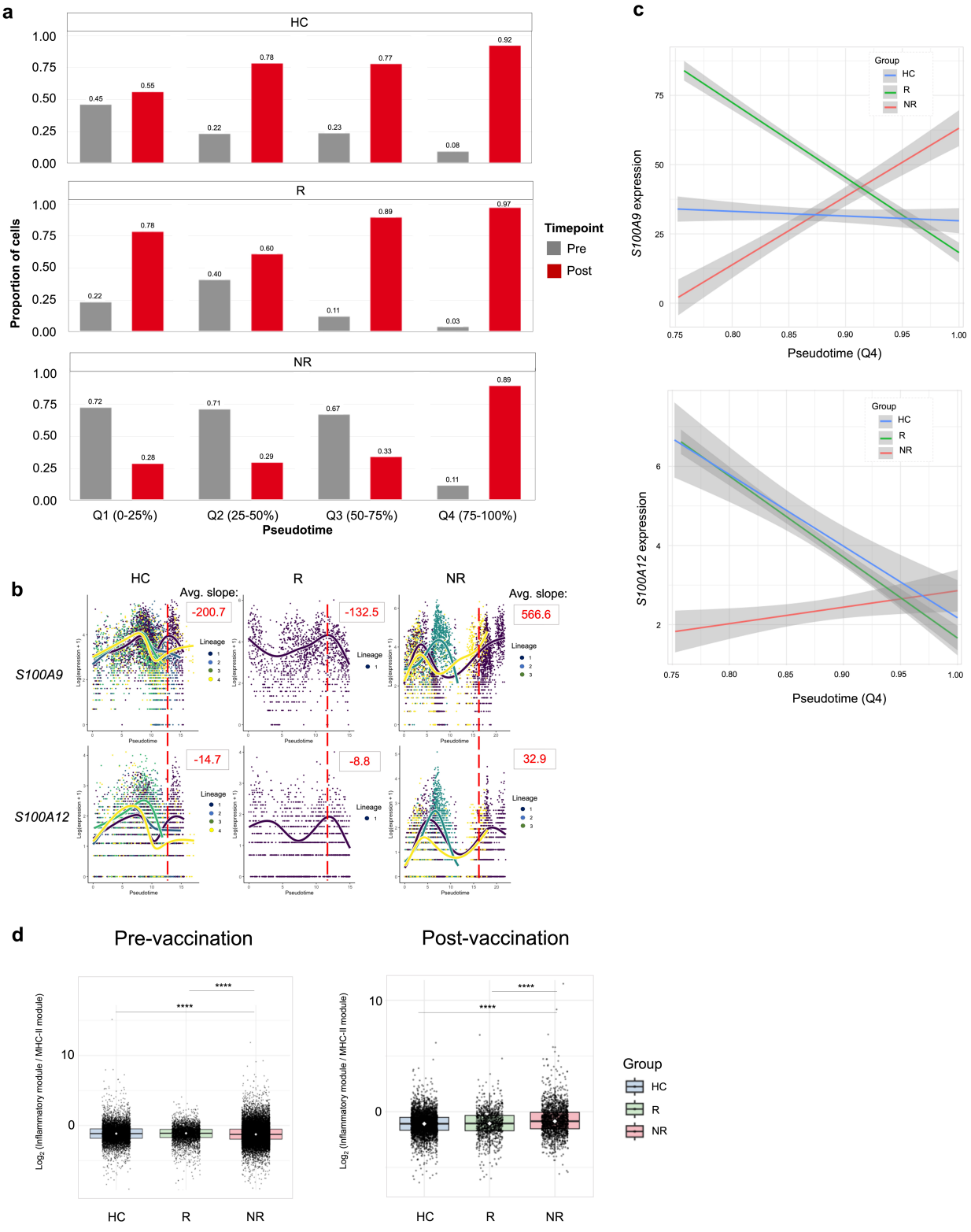

a, Bar plots showing pre- and post-vaccination changes in cell abundance along pseudotime quartiles (Q1–Q4) in healthy controls (HC), responders (R), and non-responders (NR). Each panel represents a distinct pseudotime quartile, with gray and red bars indicating pre- and post-vaccination timepoints, respectively. Values above bars indicate the mean proportion of cells in each group. **b,** Gene expression dynamics of *S100A9* and *S100A12* along monocyte pseudotime trajectories. Smoothed expression trends (colored lines) are shown for each lineage, overlaid on single-cell expression values (dots) colored by lineage identity. Red dashed vertical lines indicate the onset of the Q4 segment along each trajectory. Numeric values represent the mean slope of gene expression change within Q4. **c,** Slope of *S100A9* and *S100A12* expression trajectories within the Q4 pseudotime window across HC, R, and NR groups. Top panel shows *S100A9* and bottom panel shows *S100A12*. Lines represent linear fits of gene expression along pseudotime, with shaded areas indicating 95% confidence intervals. For *S100A9*, the slope in NR differed significantly from both HC ($P_{\text{NR vs HC}} < 2 \times 10^{-16}$) and R ($P_{\text{NR vs R}} < 2 \times 10^{-16}$). For *S100A12*, the slope in NR also differed significantly from HC ($P_{\text{NR vs HC}} < 5 \times 10^{-8}$) and R ($P_{NR\ vs\ R} = 4.6 \times 10^{-5}$). P values indicate pairwise comparisons of slope differences between groups. **d,** Box plots show log-transformed ratios of inflammatory module scores relative to MHC-II module scores in monocytes, stratified by condition (HC, R, NR) and timepoint (pre- and post-vaccination). Horizontal lines indicate median values, boxes represent interquartile ranges, and whiskers extend to 1.5× IQR. Statistical significance was determined using Wilcoxon rank-sum tests; ns, not significant.

Extended Data Fig. 4: Disrupted MHC-I and MHC-II signaling from NR monocytes to T cells.

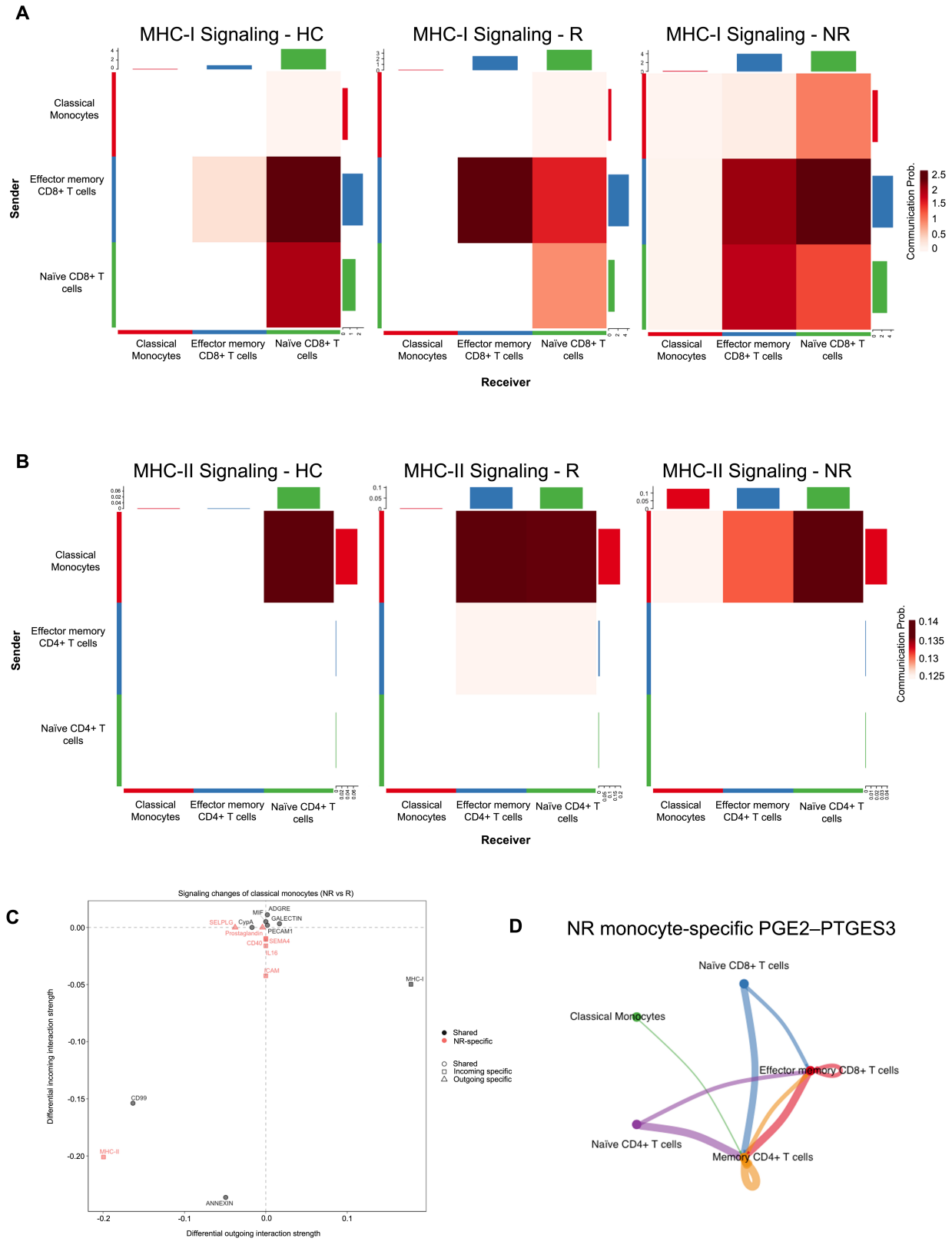

a, Heatmaps showing MHC-I signaling network strength between classical monocytes and naïve $CD8^+$ T cells in healthy controls (HC), responders (R), and non-responders (NR). **b,** Heatmaps showing MHC-II signaling network strength between classical monocytes and naïve $CD4^+$ T cells in HC, R, and NR. Network strength values were calculated using CellChat, with color intensity indicating interaction probability. **c,** Scatterplot showing differential outgoing (x-axis) and incoming (y-axis) signaling strength of classical monocytes between NR and R. NR-specific signals are highlighted in red. Point shape indicates whether the signal is shared, sender-specific, or receiver-specific. **d,** Cell–cell communication network for MHC-I signaling in non-responders. Nodes represent cell types, and edges represent inferred ligand–receptor interactions. Edge color denotes the signaling source cell type, and edge width is proportional to the communication probability.

Extended Data Fig. 5: High-dimensional Weighted Gene Co-Expression Network Analysis (hdWGCNA)-based module identification and integrative definition of a non-responder transcriptional signature.

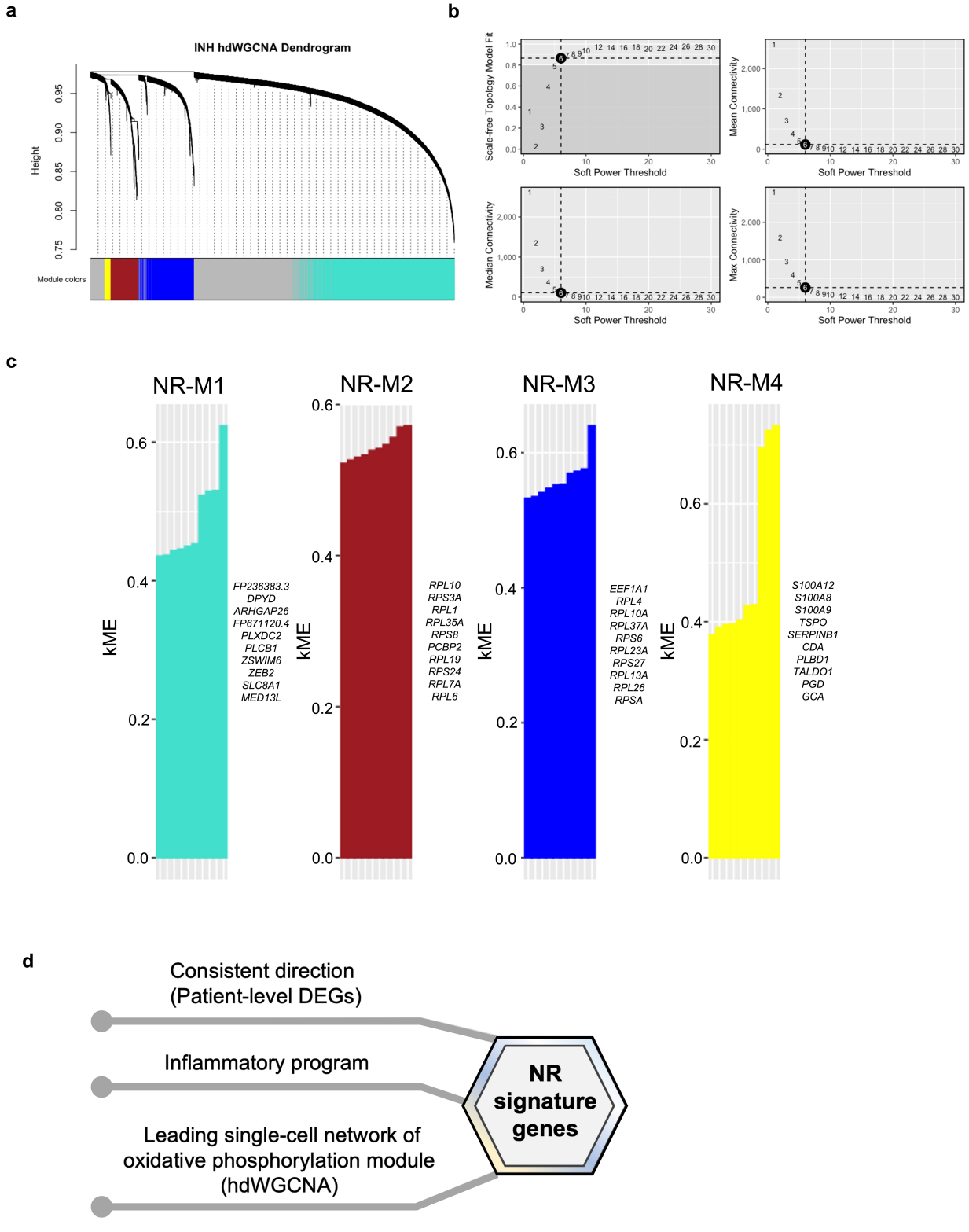

a, Hierarchical clustering dendrogram of genes constructed using hdWGCNA in classical monocytes from the pre-vaccination non-responder (NR) group. Genes were clustered based on topological overlap matrix (TOM) dissimilarity derived from a signed network (soft-thresholding power = 6). Colored bars beneath the dendrogram indicate the four identified NR-derived gene co-expression modules (NR-M1 to NR-M4), while grey represents genes not assigned to any module. **b,** Selection of the soft-thresholding power for network construction. Plots show the scale-free topology fit index (signed R^2), mean connectivity, median connectivity, and maximum connectivity across a range of candidate soft powers. A soft-thresholding power of 6 (dashed vertical line) was selected as it achieved an adequate scale-free topology fit while preserving sufficient network connectivity. **c,** Module eigengene (ME) expression profiles for the four NR-derived modules (NR-M1 to NR-M4). Bar plots display the distribution of harmonized module eigengene (hME) values across individual cells, illustrating distinct module activity patterns within the classical monocyte population. Representative genes with high module membership (kME) are annotated for each module. **d, Non-responder signature genes** were selected by integrating patient-level directional consistency, prior inflammatory and migratory annotations, and support from a single-cell oxidative phosphorylation module identified by hdWGCNA.

Extended Data Fig. 6: Gene Ontology (GO) enrichment analysis of upregulated pathways in booster-dose monocytes.

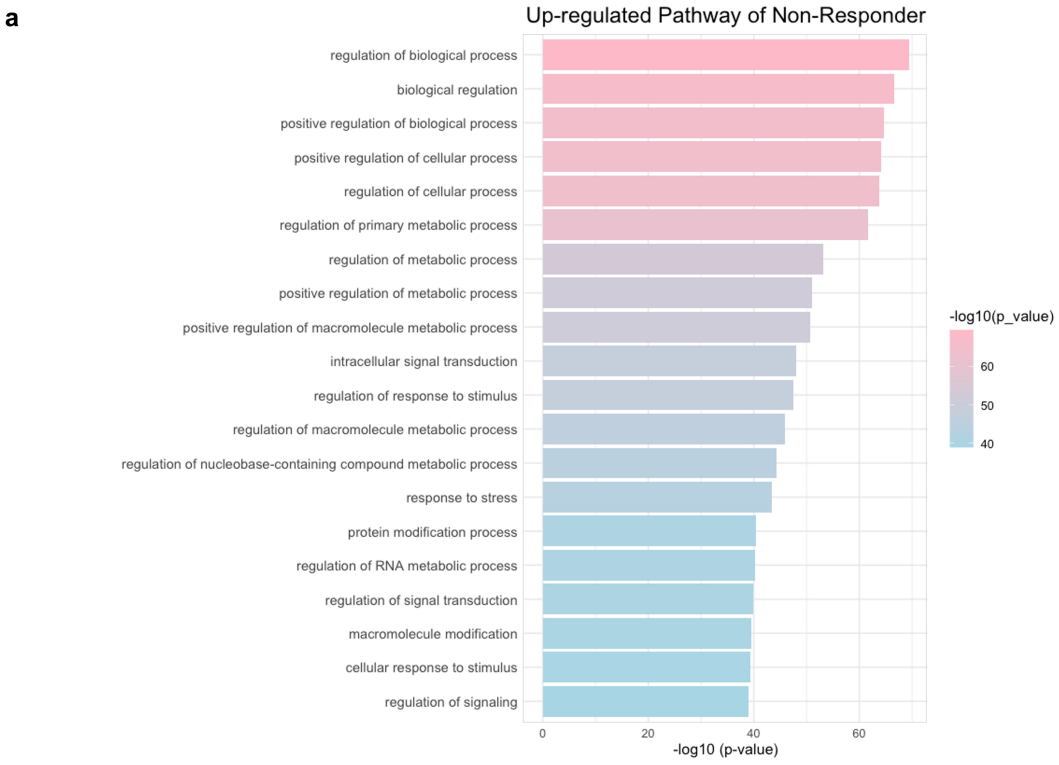

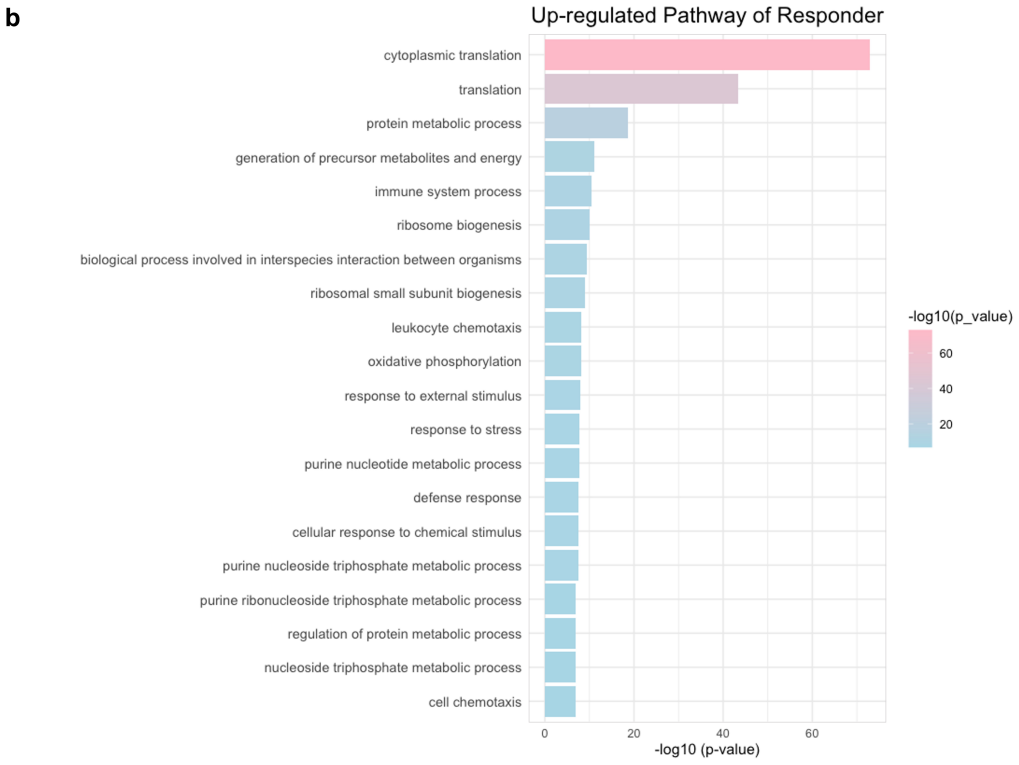

a and b, Bar plots showing significantly enriched Gene Ontology (GO) biological processes in non-responder (a) and responder (b) monocytes, based on differentially expressed genes. The x-axis indicates −log10-adjusted P values, and bar color represents adjusted P-value significance levels.

Extended Data Fig. 7: BEAM-T mapping of antigen-specific CD8⁺ T cells in responders vs non-responders.

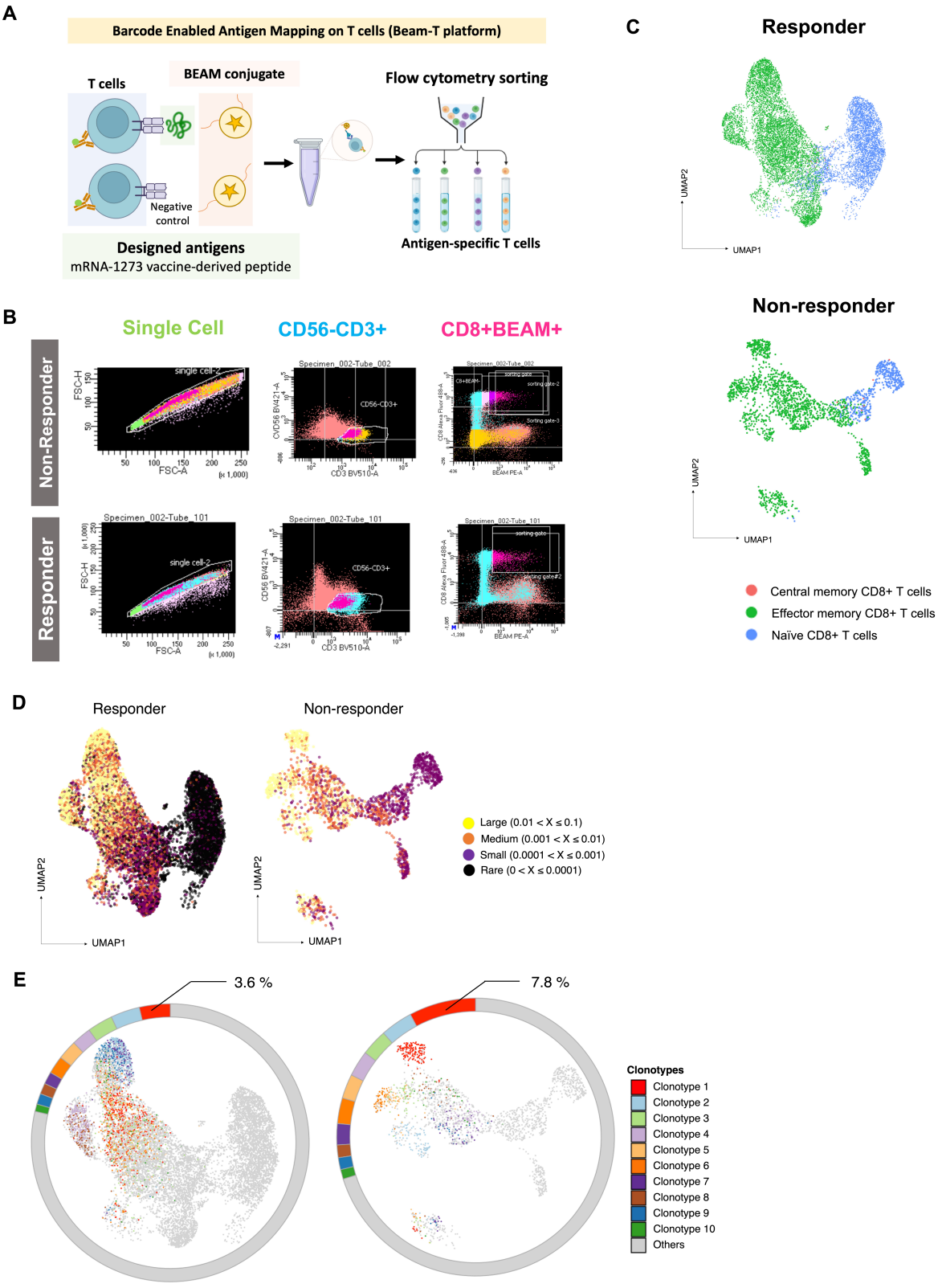

a, Schematic illustration of the Barcode Enabled Antigen Mapping on T cells (BEAM-T) platform. mRNA-1273–derived peptide antigens were conjugated to barcoded multimers and used to identify antigen-specific $CD8^+$ T cells at the single-cell level. **b,** Representative flow cytometry plots from BEAM-T profiling in NR (n=1) and R (n=1) samples, showing gating strategy for $CD8^+$ $BEAM^+$ T cells within $CD3^+CD56^-$ populations. **c,** UMAP projections of antigen-specific $CD8^+$ T cells in responders (left) and non-responders (right). Cells are colored by $CD8^+$ T cell subtype (naïve, central memory, effector memory). **d,** UMAP projections of antigen-specific $CD8^+$ T cells from responders (left) and non-responders (right), colored by TCR clone size. Bins: large (> 0.1%), medium (0.01–0.1%), small (1e−4–0.01%); the responder panel additionally includes a rare bin (< 1e−4%) as shown in the legend. TCR clonal diversity was quantified using Shannon and Simpson indices. In these two profiled cases (n = 1 per group), the NR donor showed lower Shannon diversity than the R donor (5.75 vs. 7.41), whereas Simpson diversity indices were similar (0.987 vs. 0.994). **e,** Distribution of the top 10 TCR clonotypes within antigen-specific $CD8^+$ T cells, with all remaining clonotypes of lower frequency grouped as “Other.”

Extended Data Fig. 8: XGBoost-based feature selection and trajectory analysis of pre-vaccination monocytes.

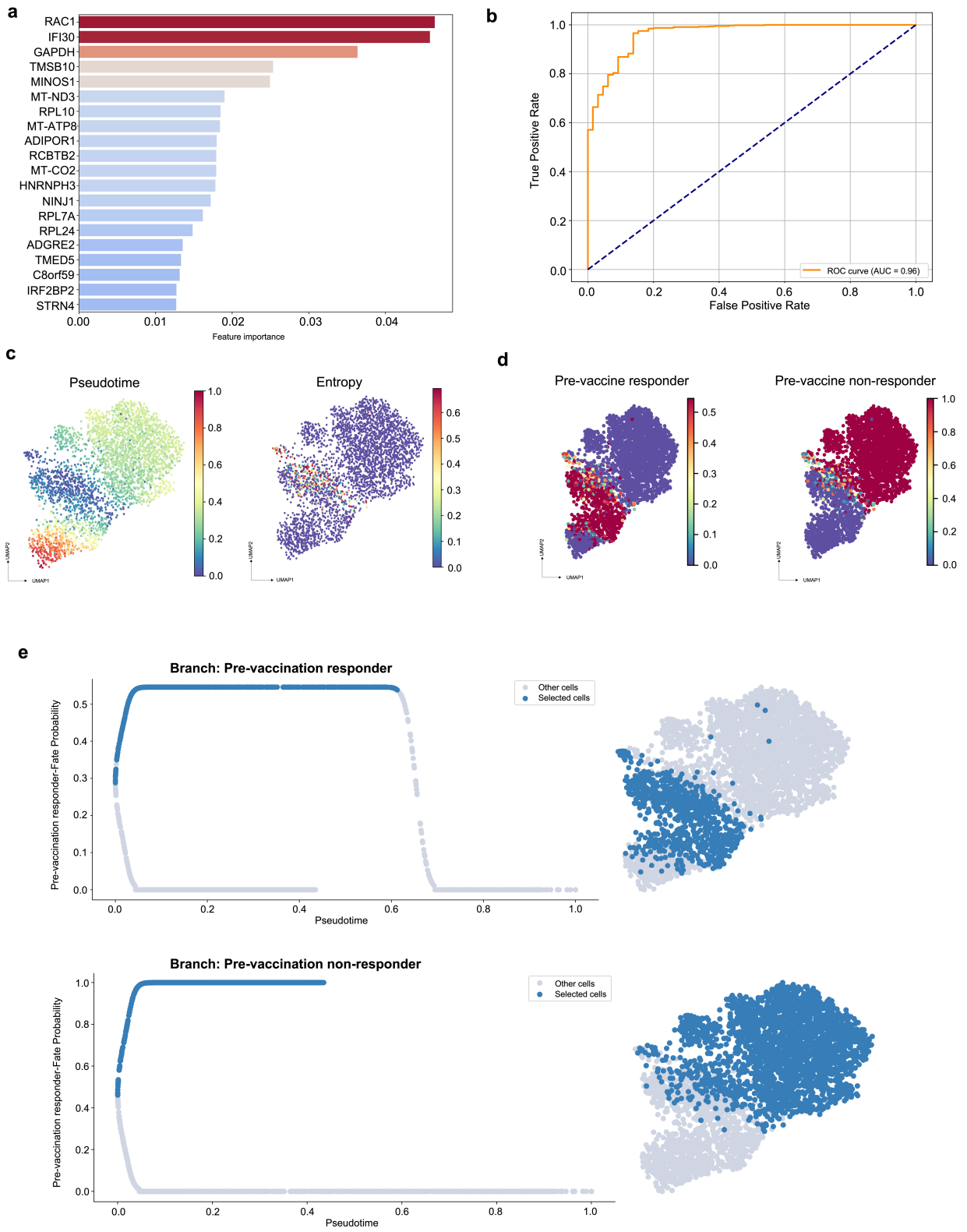

a, Top 20 most important features identified by the XGBoost classifier distinguishing non-responders (NR) from responders (R) within cluster 4 monocytes. **b,** Receiver operating characteristic (ROC) curve for the XGBoost classifier, with the area under the curve (AUC) indicated. **c,** UMAP projection of monocyte trajectories inferred by Palantir, colored by estimated pseudotime (left) and differentiation entropy (right). **d,** UMAP projections showing entropy distributions for R (left) and NR (right) monocyte lineages at pre-vaccination. **e,** Branch probability plots for R (up) and NR (bottom) monocytes, showing the likelihood of cells transitioning toward specific terminal states (left) and their corresponding UMAP locations (right).

Extended Data Fig. 9: *MT-ND3*–associated metabolic pathways and expression in independent cohort.

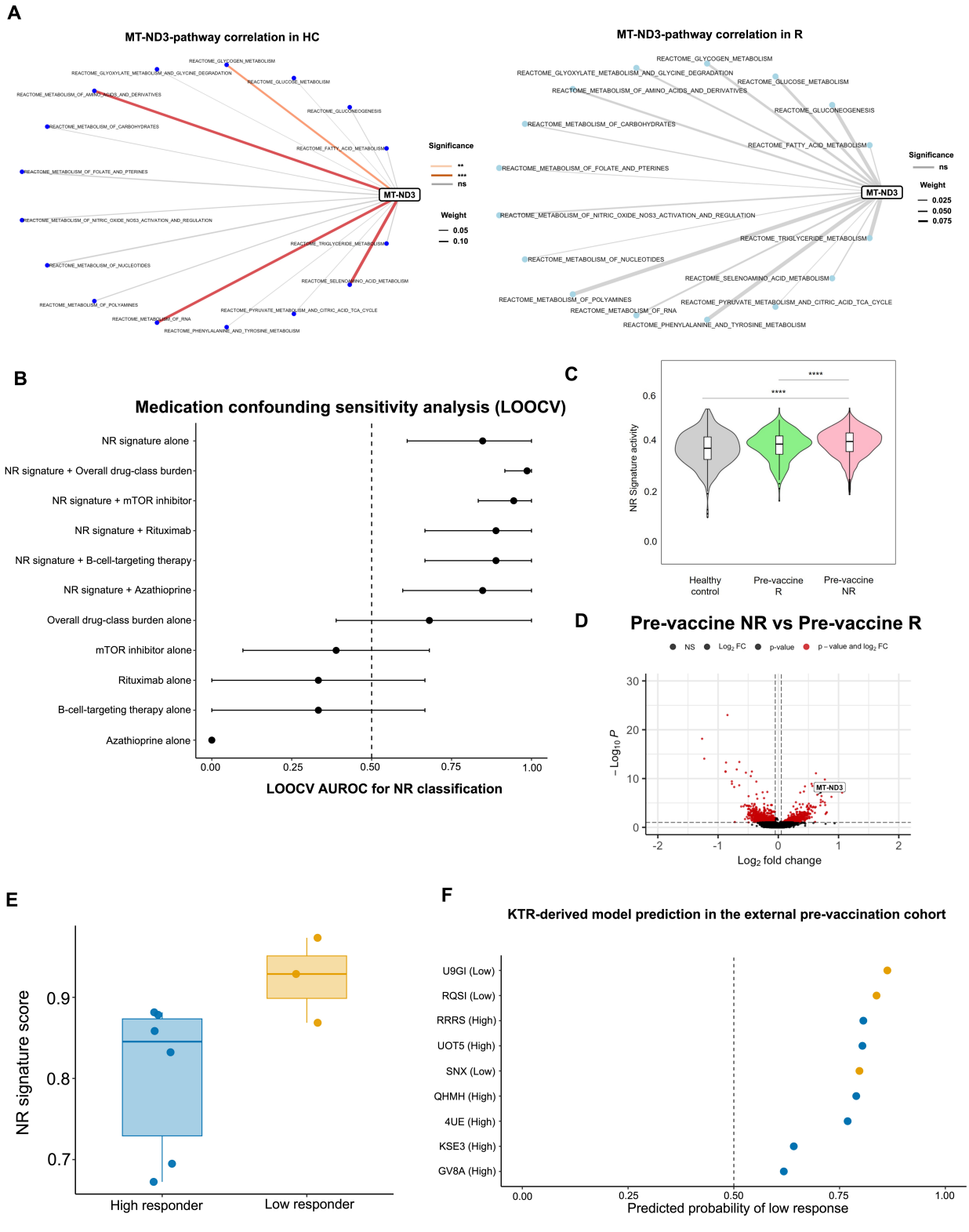

a, Correlation networks between *MT-ND3* expression and metabolic pathways in HC (left) and R (right) at pre-vaccination. Edge thickness indicates correlation strength; color denotes significance level. **b,** Medication-confounding sensitivity analysis. Donor-level LOOCV models compared the NR signature with several recorded medication variables and overall drug-class burden for non-responder classification. Overall drug-class burden was defined as the number of recorded immunosuppressive drug classes per donor, including calcineurin inhibitors, mycophenolate/MPA, corticosteroids, mTOR inhibitors, azathioprine, ATG/ALG, and B-cell-targeting therapy. Points indicate LOOCV AUROC values, horizontal bars indicate 95% confidence intervals, and the dashed vertical line marks AUROC = 0.5. **c,** Violin plots showing NR module signature activity score in healthy controls, NR, and R at pre-vaccination in the independent cohort. Horizontal bars indicate statistical significance (P values from Wilcoxon rank-sum test). **d,** Volcano plot of differential gene expression between NR and R at pre-vaccination in the BNT independent cohort, highlighting *MT-ND3.* **e,** External pre-vaccination NR-signature scores by response group. Box plot showing raw NR-signature scores in pre-vaccination samples from an external healthy BNT162b2 low/high responder cohort (GSE246937). Each point represents one donor sample. **f,** Application of the fixed KTR-derived model to an external pre-vaccination cohort. The KTR-derived model was applied to pre-vaccination samples from an external healthy BNT162b2 low/high responder cohort without external refitting, recalibration, cohort-specific scaling, or threshold optimization. Each point represents one donor sample and shows the predicted probability of low response. The model discriminated low from high responders with AUROC = 0.889 and AUPRC = 0.867. The dashed vertical line marks a predicted probability of 0.5.

Extended Data Fig. 10: Gene regulatory network–based perturbation simulation with CellOracle.

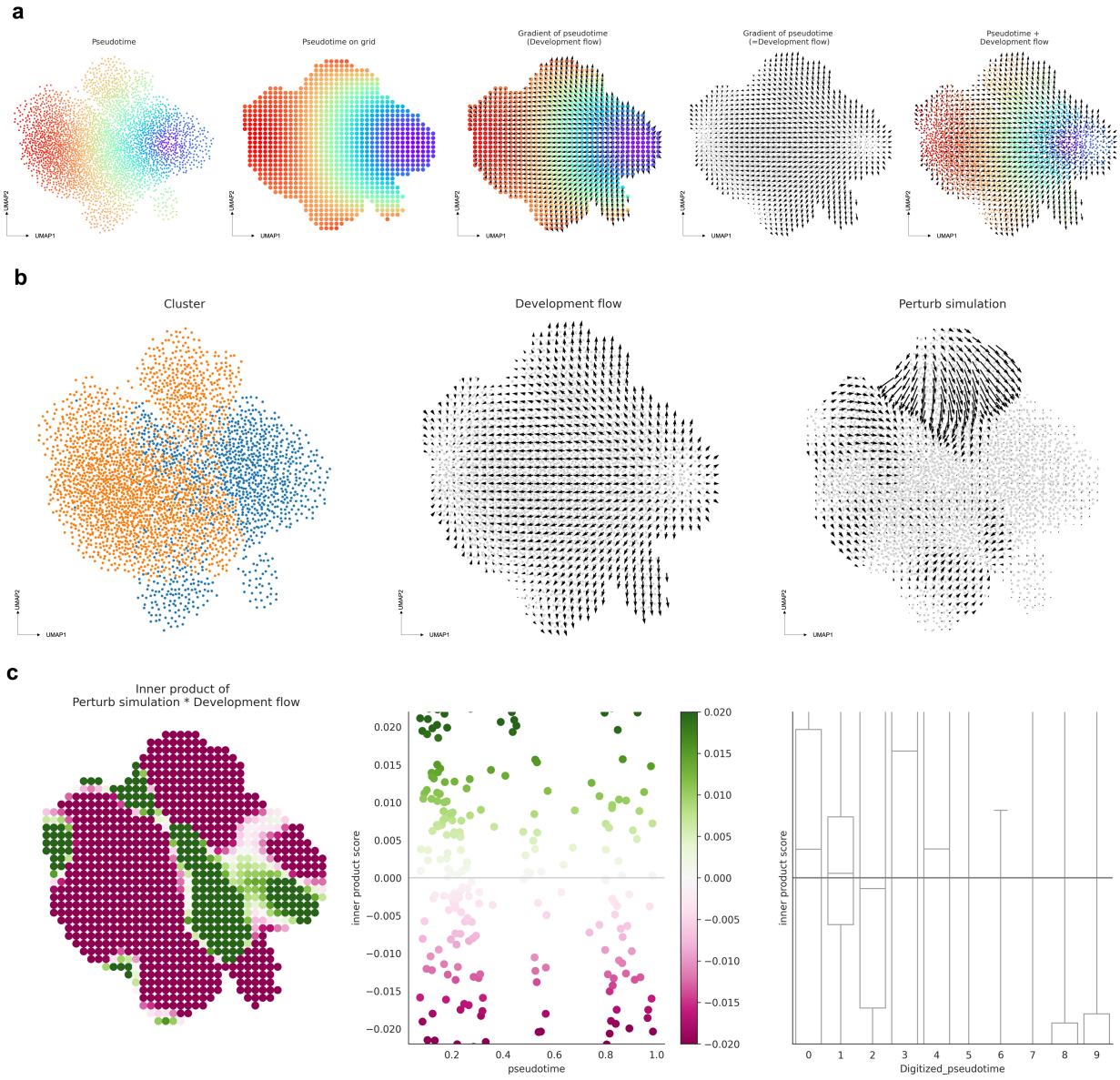

a, Pseudotime and trajectory inference results from CellOracle, showing pseudotime ordering, pseudotime grid, and developmental flow vectors overlaid on the cell embedding. **b,** Gene regulatory network (GRN)–based perturbation analysis for the indicated condition. Left to right: cell clusters, inferred developmental flow, and simulated developmental flow after in silico perturbation of *FOXO1*. **c,** Quantification of perturbation effects. Left: spatial distribution of the inner product between perturbation simulation and developmental flow vectors, with positive values (green) indicating alignment and negative values

(magenta) indicating reversal of trajectory direction. Middle: scatterplot showing inner product values across pseudotime. Right: boxplot summarizing inner product values across digitized pseudotime bins.

Extended Data Fig. 11: External validation of non-responder monocyte signature across immunocompromised conditions.

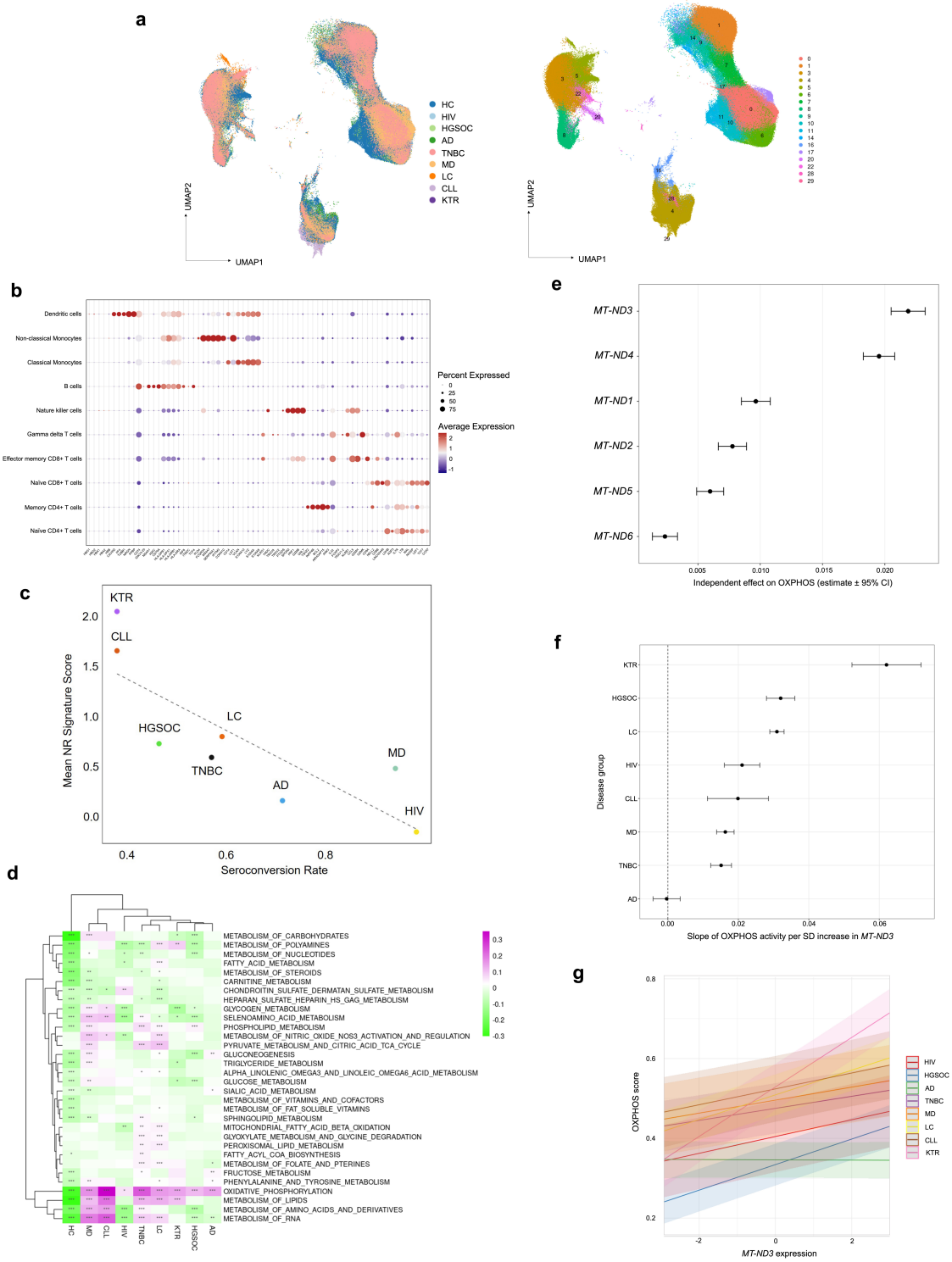

a, UMAP projection of integrated 237,534 single-cell transcriptomes from kidney transplant recipients (KTR) and additional immunocompromised (IC) conditions, colored by clusters. **b,** Dot plot of selected marker genes across major immune cell populations. Dot size indicates the proportion of cells expressing the gene, and color intensity reflects average expression. **c,** Scatter plot showing the mean NR signature score in monocytes (y-axis) versus reported mRNA vaccine seroconversion rates (x-axis) across immunocompromised conditions. Each point represents one IC group: KTR, chronic lymphocytic leukemia (CLL), lung cancer (LC), high-grade serous ovarian cancer (HGSOC), triple-negative breast cancer (TNBC), autoimmune diseases (AD), metabolic disease (MD), and HIV. The dashed line indicates the negative association between NR signature enrichment and seroconversion. **d,** Heatmap showing correlations between the NR monocyte signature and curated metabolic pathways across IC conditions. Color scale represents correlation coefficients, with positive values (purple) indicating pathways aligned with the NR signature and negative values (green) indicating inverse associations. **e,** Independent contribution of mitochondrially encoded complex I genes to OXPHOS activity. Independent effects of mitochondrially encoded complex I genes on monocyte OXPHOS activity were estimated using linear mixed-effects models adjusting for mitochondrial percentage, library size, and disease group, with a random intercept for sample identity. Effect sizes correspond to standardized regression coefficients for each *MT-ND* gene while adjusting for all included variables. Ninety-five percent confidence intervals were calculated from model-based standard errors. *MT-ND3* had an estimated effect size of 0.021 ± 0.003. **f,** Variation in *MT-ND3*-OXPHOS coupling strength across immunocompromised conditions. Disease-specific *MT-ND3*-OXPHOS coupling coefficients were obtained using interaction models incorporating *MT-ND3* expression, disease group, mitochondrial percentage, library size, and a random intercept for sample identity. Slopes represent the predicted change in OXPHOS activity per one standard deviation increase in *MT-ND3* within each disease group. Error bars indicate ninety-five percent confidence intervals. **g,** Model-derived predicted values illustrating *MT-ND3*–OXPHOS relationships across disease groups. Predicted OXPHOS activity was computed using a linear mixed-effects model including *MT-ND3* expression, disease group, mitochondrial percentage, library size, and a random intercept for sample identity. Lines and shaded

intervals represent model-derived predictions and ninety-five percent confidence bands for each disease group across the observed range of *MT-ND3* expression.

Supplemental Methods

Study design

To investigate innate determinants of vaccine non-responsiveness, we performed single-cell RNA sequencing (scRNA-seq) of classical monocytes isolated from peripheral blood mononuclear cells (PBMCs) in kidney transplant recipients. The study aimed to (i) define monocyte-intrinsic transcriptional and metabolic states associated with vaccine non-responsiveness; (ii) investigate how these states influence innate–adaptive immune coordination and downstream T cell outcomes; (iii) identify predictive molecular markers and therapeutic candidates capable of reversing monocyte dysfunction. A total of 43 PBMC samples containing non-responder (NR) and responder (R) were analyzed, including paired pre-vaccination samples from kidney transplant recipients (KTRs), with 9 pre-vaccination non-responder samples, 8 pre-vaccination responder samples, 13 post-vaccination non-responder samples, and 13 post-vaccination responder samples, from kidney transplant recipients immunized with the primary dose of mRNA-1273. 38 healthy control samples were obtained from our in-house dataset and publicly available datasets on the GEO database. For validation, an independent cohort dataset was integrated, consisting of in-house booster dose samples of 4 NR, 8 R, and 11 vaccinated healthy controls from GSE260763. This validation dataset was applied to assess whether the identified non-responder phenotypes persist after booster vaccination, further reinforcing the durability of immune dysfunction in vaccine non-responders.
All samples were processed using 10X Genomics droplet-based 3' scRNA-seq, allowing for high-resolution profiling of innate immune monocyte subsets. Clinical and demographic details are provided in Supplemental Tables 1 and 2.

Sample collection

Kidney transplant recipients (KTRs) were recruited from Taichung Veteran Hospital, with inclusion criteria requiring age ≥18 years, stable graft function, and no active infections. Peripheral blood samples were collected from KTRs at two time points: pre-vaccination and within 30 days post-administration of mRNA-1273 (Moderna COVID-19 vaccine). Non-responders (NR) and responders (R) were classified based on antibody levels measured using the Roche Elecsys Anti-SARS-CoV-2 S assay, with a threshold of <0.4 BAU/mL (Binding Antibody Units per milliliter) defining non-responsiveness (Supplementary Table 17). Samples were collected between July 2021 and May 2022 as part of a longitudinal study assessing immune responses to mRNA vaccination in immunocompromised individuals. Healthy controls (HCs) were included as baseline comparators incorporated by the in-house dataset and the following publicly accessible datasets: GSE240694, GSE216064, GSE244515, GSE231794, GSE181543, GSE206283, GSE199994 and GSE260763 (64-71). Metadata from these datasets were reviewed to ensure consistency in sample preparation, sequencing protocols, and study design.

scRNA-seq and CITE-seq library preparation and sequencing

Peripheral blood mononuclear cells (PBMCs) were labeled with oligonucleotide-barcoded antibodies from the TotalSeq™-C antibody panel (BioLegend, San Diego, CA) to enable simultaneous quantification of surface protein expression and transcriptomic profiles. The antibody panel included markers for major immune lineages and immunoregulatory pathways, including CD3 (C0049), CD4 (C0072), CD8a (C0080), CD14, CD16 (C0083), CD19, CD45RA (C0063), CD45RO, CD25 (C0085), CD127 (C0390), CD64 (C0162), CD56 (C0084), CD24 (C0180), CD27 (C0154), CD69 (C0146), CD73 (C0577), CD103 (C0145), CD183 (CXCR3, C0140), CD197 (CCR7, C0148), CD194 (CCR4, C0071), and checkpoint molecules PD-1 (CD279), PD-L1 (CD274, C0007), CD152 (CTLA-4, C0151), CD366 (Tim-3, C0169), and TIGIT. Additional markers included HLA-ABC (C0058), HLA-DR (C0159), CD11c, CD44 (C0125), CD31 (C0124), CD72 (C0419), CD79b (C0187), CD2 (C0367), CD39 (C0176), CD94 (C0867), CD74 (C0935), and appropriate IgG isotype controls (C0090–C0092). Antibody-labeled samples were loaded onto a 10X Genomics microfluidics chip and encapsulated with barcoded hashtag oligos (HTOs)-containing gel beads using the 10X Genomics Chromium Controller. Within each droplet, single cells underwent lysis, releasing

mRNAs that were captured by the barcoded gel beads and converted to barcoded complementary DNAs (cDNAs). The barcoded cDNAs from HTOs and mRNAs were pooled and subsequently prepared into single-cell RNA sequencing (scRNA-seq) libraries using the Chromium Single Cell 3' Reagent Kit (10X Genomics, Pleasanton, CA). The libraries were sequenced using an Illumina platform, enabling high-resolution transcriptomic profiling and antibody-derived tag (ADT) quantification for sample demultiplexing.

scRNA-seq and CITE-seq data processing

The raw FASTQ files were processed using Cell Ranger Software (v7.0.0, 10X Genomics) for alignment and quantification against the GRCh38 human transcriptome (v3.0.0) (72). Empty droplets were excluded through Cell Ranger's built-in quality control algorithms. Cells were filtered based on quality criteria, retaining those with 200 to 4000 detected genes and excluding cells with mitochondrial gene content exceeding 5% of total reads. To ensure the retention of high-confidence singlets for downstream analysis, Hashtag Oligo (HTO) demultiplexing was performed. Cells were categorized as singlets, doublets, or unmapped, and only singlets were retained for subsequent analysis to minimize noise and avoid artifacts. Singlets were extracted from the Seurat object using the subset function. The metadata column storing HTO assignments (HTO_maxID) was standardized by converting it into a factor with defined levels corresponding to the experimental HTO barcodes. Normalization of gene expression counts was performed using the Seurat function **NormalizeData**, applying a scale factor of 10,000 followed by natural log transformation. Highly variable genes (HVGs) were identified using the **FindVariableFeatures** function with the "vst" method, selecting the top 2000 variable genes. These HVGs were subsequently scaled and centered based on their expression values to ensure comparability across cells. The processes were performed by Seurat with version 3.1.4.

Dimension reduction and unsupervised clustering

For Seurat-based analysis, normalized data were subjected to principal component analysis (PCA) using the RunPCA function to reduce the dimensionality of the dataset. The top 10 principal components (PCs) were initially selected based on the elbow plot for downstream clustering. To further address potential batch effects, the harmony integration method was applied with a dimensionality reduction parameter set to 30. Harmony-corrected embeddings were then used for clustering and visualization. Uniform manifold approximation and projection (UMAP) was performed using the RunUMAP function with the top 30 harmony-corrected dimensions. Clustering was performed using the Louvain algorithm via the FindClusters function, with a resolution parameter set to 0.5. For the scvi-tools approach (v1.2.0) (73), raw count data were normalized using a deep generative model to correct for batch effects and integrate datasets across experimental conditions. The scvi.model.SCVI module was used to train the variational autoencoder on all cells, incorporating batch annotations as covariates to account for technical variability. Following model training, the latent embeddings were extracted and used for UMAP visualization with scanpy.tl.umap. Leiden clustering was performed on the latent space using scanpy.tl.leiden, with a resolution parameter optimized to capture biologically meaningful clusters. This framework enabled unbiased integration of batch-corrected datasets for robust clustering and lineage inference.

Clustering and immune cell type annotation

After quality control filtering to exclude doublets and low-quality cells, a total of 438,088 peripheral blood mononuclear cells (PBMCs) were analyzed. Unsupervised clustering was performed using Seurat (v4.3.0) (74) with Louvain-based modularity optimization at a resolution parameter of 0.5, identifying 30 initial clusters. To assign cell type identities, the SingleR package (v1.4.1) was first applied, leveraging reference transcriptomes to perform preliminary annotation (75). Subsequently, cluster labels were refined based on transcriptome-wide RNA expression, coordinated multi-gene marker profiles, and cluster-level differentially expressed genes (DEGs) identified using the FindAllMarkers function in Seurat, followed by

manual cross-referencing with established lineage-associated markers. ADT measurements were used as complementary validation for selected surface phenotypes rather than as the primary basis for cell-type annotation. Major immune cell types were classified, including eight T cell subsets (characterized by CD3E expression), three monocyte populations (marked by *VCAN* expression), one natural killer (NK) cell population (marked by *NCAM1*), and one B cell population (marked by *CD79A*) (76-78). The initially annotated classical monocyte population was computationally subset from the whole-PBMC dataset and subjected to secondary reclustering This higher-resolution analysis was performed to resolve transcriptional heterogeneity within the classical monocyte population. Cluster identities were assigned using the same RNA-based annotation strategy, integrating coordinated multi-gene expression patterns and cluster-level DEGs. Higher-resolution subclustering of resolved four transcriptionally distinct states: classical monocytes (expressing high levels of *CD14*, *LYZ*, and *S100A9*) macrophage-like monocytes (expressing *CD83*, *TNF*, *IL1B*), intermediate monocytes (expressing *FCGR3A*, *CCR5*, *PRF1*), DC-like monocytes (expressing *TNFAIP3*, *CD69*, *CCR7*), and undifferentiated classical monocytes (expressing high levels of *CD14*, *LYZ*, and *S100A9*) (79-84). ADT measurements, where informative, were used to support selected surface-protein phenotypes of these states.

Quantification of immune–metabolic coherence

To identify monocyte populations with transcriptionally aligned metabolic and antigen-presenting programs, we defined a functional coherence score that integrates the directionality and dispersion of gene–gene correlations between mitochondrial and antigen presentation genes. Specifically, for each monocyte group *k*, we calculate the Spearman correlation coefficient $\rho_{ij}^{(k)}$ between mitochondrial genes ($i \in M$) and antigen presentation genes ($j \in A$) across cells, based on single-cell expression vectors $x_i^{(k)}$ and $x_j^{(k)}$ as equation (1):

$$\rho_{ij}^{(k)} = \text{Spearman}\left(x_i^{(k)}, x_j^{(k)}\right) \tag{1}$$

We then quantified the directionality consistency of these correlations by computing the proportion of positively correlated gene pairs as equation (2):

$$p_+^{(k)} = \frac{1}{|M||A|} \sum_{i \in M} \sum_{j \in A} I\left(\rho_{ij}^{(k)} > 0\right) \tag{2}$$

To assess the variability in correlation direction, we calculated the Shannon entropy of the correlation sign distribution as equation (3):

$$H^{(k)} = -\sum_{s \in \{+,-\}} p_s^{(k)} \log_2 p_s^{(k)} \tag{3}$$

Where $p_s^{(k)}$ denotes the fraction of the gene pairs with sign $s \in \{+,-\}$. Finally, we defined a coherence score to prioritize monocyte groups with consistently aligned immune-metabolic programs as equation (4):

$$Coherence^{(k)} = \frac{p_+^{(k)}}{H^{(k)}} \tag{4}$$

Higher scores indicate more consistent and coordinated transcriptional coupling between metabolic and antigen-presenting programs, which reflects a metabolically aligned immune state.

Differential expression analysis, module scoring, and pathway enrichment

Multiple immune and metabolic gene programs were quantified using the AddModuleScore function in Seurat, including inflammatory and antigen-presenting modules, as well as the curated NR-focused gene sets computed and projected onto the booster cohort to evaluate their predictive capacity. GO enrichment

analysis was conducted to identify functional categories associated with NR- and R-specific DEG gene sets. GO term mapping was performed using the gProfiler2 package (v0.2.3) in R (85), with significance determined based on an adjusted p-value < 0.05 (Benjamini-Hochberg correction). Enriched biological processes were further analyzed using the clusterProfiler package (v4.12.6) and the org.Hs.eg.db human gene annotation database (v3.19.1) (86). Enrichment results were visualized using bar plots (generated with ggplot2 v3.5.2), where the −log10 (adjusted p-value) was plotted against GO terms.

Feature selection

Feature selection was conducted using the XGBoost classifier to identify critical genes differentiating non-responders (NR) and responders (R) from their expression profiles in classical monocytes (87). Analysis was performed in Python (v3.8.5) utilizing the XGBoost (v2.1.2), scikit-learn (v1.5.2), pandas (v2.2.3), and numpy (v1.26.3) libraries. Gene expression matrices derived from classical monocytes were preprocessed by scaling using StandardScaler to normalize feature distributions. The dataset was randomly split into training (80%) and testing (20%) subsets while maintaining balanced class proportions. The XGBoost model was configured for binary classification with the objective function set to binary:logistic. To address class imbalance between NR and R groups, the scale_pos_weight parameter was dynamically assigned based on the ratio of negative to positive samples in the training set. Hyperparameter optimization was conducted via grid search, tuning n_estimators, max_depth, learning_rate, subsample, and colsample_bytree parameters. The best-performing model was selected based on cross-validated accuracy. Model performance was evaluated using standard metrics, achieving high predictive accuracy (accuracy: 0.96, precision: 0.97, recall: 0.99, F1-score: 0.98), with an area under the receiver operating characteristic curve (AUC-ROC) of 0.96, indicating robust classification ability. Feature importance scores were extracted using XGBoost's built-in feature_importances_ attribute, ranked in descending order, and the top 20 predictive genes were identified. Visualization of feature contributions was generated using Matplotlib (v3.9.2) and Seaborn (v0.13.2)

High-dimensional Weighted Gene Co-Expression Network Analysis (hdWGCNA)

To identify co-expression programs associated with vaccine responsiveness in classical monocytes, hdWGCNA (v0.4.00) was performed using a Seurat-based workflow (88). Briefly, the Seurat object was prepared for network analysis using SetupForWGCNA, where genes were selected by an expression-frequency criterion ("fraction"), retaining genes expressed in at least 5% of cells (fraction = 0.05). To reduce sparsity and improve network robustness, metacells were constructed within each condition group (condition2) using a KNN graph built on the Harmony-corrected UMAP embedding (k = 25), restricting metacell overlap to a maximum of 10 shared cells (max_shared = 10). Metacell expression matrices were then normalized with NormalizeMetacells. For network construction, the normalized RNA assay data layer (assay = "RNA", layer = "data") was used to define the expression matrix (SetDatExpr) for the "Pre-vaccination non-responder" group within condition2 metadata label. A signed co-expression network was built, with the soft-thresholding power fixed at 6 (networkType = "signed"), and the adjacency matrix was transformed into a topological overlap matrix (TOM; tom_name = "NR"). Genes were hierarchically clustered based on TOM dissimilarity to define modules, and the resulting gene dendrogram was visualized to assess module structure. Module eigengenes (MEs) were computed on the full single-cell dataset using ModuleEigengenes with harmonization across condition2, enabling downstream comparisons of module activity while accounting for condition-level effects.

Module membership and intramodular connectivity were quantified by eigengene-based connectivity (kME) using ModuleConnectivity, focusing on the "Pre-vaccination non-responder" group. Modules were renamed with the prefix "NR-M" (ResetModuleNames) for consistent reporting, and hub genes were defined as the top-ranked genes by kME (top 10 per module; GetHubGenes). For module–trait association testing in classical monocytes, cells were subset by identity ("Classical Monocytes"), and condition dummy variables were constructed with Healthy control as the reference (cond_R for pre-vaccination responder; cond_NR for pre-vaccination non-responder). Pearson correlations between harmonized MEs and these

traits were calculated, and multiple testing correction was performed using FDR across all module–trait tests; results were visualized as correlation heatmaps annotated with effect size (r) and q-values (FDR). Finally, module assignment tables were exported after excluding unassigned "grey" genes, and gene members of selected modules, defined as those showing a positive correlation with the non-responder trait ($r \geq 0.25$) and a concurrent negative correlation with the responder trait ($r \leq -0.05$; FDR-adjusted $q < 0.05$) were extracted for downstream analyses.

Trajectory analysis with Palantir

Trajectory analysis was performed using Palantir (v1.3.3) (89) to model the progression of classical monocytes from healthy controls, pre-vaccination non-responders (NR), and pre-vaccination responders (R). The single-cell RNA sequencing (scRNA-seq) dataset was preprocessed using Scanpy (v1.10.2) before being analyzed with Palantir. Specifically, data normalization was applied per cell, followed by log transformation and identification of 2500 highly variable genes. Principal component analysis (PCA) was conducted and compute the diffusion maps, which form the basis for pseudotime estimation. To identify the root cell, cells from healthy controls were designated as the starting population. Terminal states corresponding to non-responder and responder phenotypes were defined using the terminal_states parameter, and trajectory inference was conducted using 1000 waypoints to optimize the sampling resolution. Gene expression trends along the inferred trajectories were imputed using MAGIC, ensuring the robustness of pseudotime-dependent gene expression profiles. The imputed data were visualized using UMAP, highlighting pseudotime progression and branch probabilities. Terminal probabilities were plotted to identify lineage-specific distributions toward NR or R phenotypes, and branch-specific cell subsets were selected using Palantir's select_branch_cells functionality. Marker gene expression trends were computed using the compute_gene_trends function, and pseudotime trajectories were visualized with arrow-based projections to represent differentiation directionality. Key trajectory-based insights were further integrated with functional gene analyses to elucidate distinct lineage-driving mechanisms. All visualizations were generated using Matplotlib (v3.9.2). Importantly, this approach was designed to assess relative progression across HC, NR, and R, rather than to benchmark canonical developmental hierarchies.

Trajectory inference with Slingshot and TradeSeq

To infer cellular trajectories from pre- to post-vaccination states, Slingshot (v2.12.10) and tradeSeq (v1.18.0) were applied in R (90, 91). The dataset was first normalized, scaled, and clustered using Seurat (v4.4.1). Principal component analysis (PCA) was performed, and the first 20 principal components were selected for uniform manifold approximation and projection (UMAP) embedding. Clusters were identified, and a biologically relevant cluster was designated as the starting population for trajectory inference. Lineage reconstruction was conducted using Slingshot, with cluster labels serving as input and UMAP coordinates as the reduced dimension for trajectory computation. Lineage structures were extracted using slingLineages, and smooth trajectory curves were generated using slingCurves. Pseudotime values were assigned to individual cells based on their positions along the inferred trajectories, enabling the reconstruction of monocyte differentiation states from pre- to post-vaccination. To investigate gene expression dynamics along pseudotime, tradeSeq was employed. A generalized additive model (GAM) was fitted to count data using the fitGAM function, with pseudotime as a continuous predictor. The associationTest function was used to identify differentially expressed genes (DEGs) exhibiting significant expression variation along the inferred trajectories, with genes ranked based on adjusted p-values. Additionally, differential gene expression at the terminal states of each trajectory was assessed using diffEndTest, and the most significant genes were visualized using plotSmoothers and plotGeneCount. Importantly, this approach was designed to assess relative progression across HC, NR, and R, rather than to benchmark canonical developmental hierarchies.

Pathway activity estimation using AUCell

Pathway activity scores were computed using AUCell (v1.26.0) to assess gene set enrichment at the single-cell level (92). First, the gene expression matrix was extracted from the RNA assay and used to construct cell-specific gene expression rankings with AUCell_buildRankings, where genes were ranked based on their expression levels within each cell. Next, AUCell_calcAUC was applied to calculate the Area Under the Curve (AUC) scores for predefined gene sets, reflecting the relative enrichment of each pathway. AUC scores were extracted using getAUC and assigned to individual cells for downstream analyses. To visualize pathway activity across different conditions, heatmaps were generated based on AUC matrices, Heatmaps were generated from the AUC matrices to display pathway activity across different conditions through pheatmap (v1.0.12).

Gene Set Enrichment Analysis (GSEA)

Gene Set Enrichment Analysis (GSEA) was performed using fgsea (v1.30.0) to identify significantly enriched pathways in different monocyte subpopulations. Differentially expressed genes (DEGs) were identified between specified conditions using FindMarkers with no log fold change threshold and a minimum percentage of expression cutoff set to zero. Gene ranking for GSEA was based on the log-fold change values, and ranked gene lists were generated for each comparison. The fgsea function was applied to the ranked gene lists using predefined gene sets, with pathway size constraints set between 3 and 15,000 genes and nperm set to 15,000 for statistical robustness.

Cell-cell communication signaling pathway analysis

Cell-cell interaction networks were inferred using CellChat (v2.1.2) to examine ligand-receptor interactions among monocyte subsets (93). The Seurat object was used as input, and cell type identities were assigned as metadata. The createCellChat function was applied to construct the CellChat object, followed by the selection of the CellChatDB.human database for human ligand-receptor interactions. Overexpressed genes and interactions were identified using identifyOverExpressedGenes and identifyOverExpressedInteractions, respectively. The communication probability was computed using computeCommunProb, applying the "triMean" method, and low-confidence interactions were filtered based on a minimum cell count threshold of 10 using filterCommunication. To evaluate signaling pathways, computeCommunProbPathway was used to infer pathway-level communication, and aggregateNet was applied to generate the aggregated interaction network. The strength and frequency of interactions were visualized using netVisual_circle, depicting both the number of interactions and interaction weights across different monocyte subsets. Differential communication patterns between conditions were assessed using netVisual_diffInteraction, highlighting shifts in network connectivity.

For comparative analysis, CellChat objects from different groups (e.g., non-responders, responders, and healthy controls) were merged using mergeCellChat. Interaction frequencies and signal strengths were compared using compareInteractions across conditions. Heatmaps of signaling pathway activity were generated with netVisual_heatmap, and edge weights were normalized across datasets using getMaxWeight. Network centrality measures were computed using netAnalysis_computeCentrality, followed by role classification of monocyte populations through netAnalysis_signalingRole_heatmap and netAnalysis_signalingRole_scatter. The overall contribution of each signaling network was quantified using rankNet, ranking the dominant ligand-receptor pairs influencing immune communication dynamics.

Barcode Enabled Antigen Mapping of T Cells (BEAM-T)

To characterize antigen-specific $CD8^+$ T cell responses following mRNA-1273 vaccination, we employed Barcode Enabled Antigen Mapping of T Cells (BEAM-T), a single-cell multi-omics platform that enables high-resolution profiling of TCR clonality and transcriptional states in response to defined antigens (10x Genomics, Pleasanton, CA; https://www.10xgenomics.com/support/software/cell-ranger/latest/analysis/running-pipelines/cr-5p-antigen). A custom library of mRNA-1273–derived peptides was designed using NetMHCpan 4.1, selecting 10mer peptides with high predicted binding affinity to prevalent HLA class I alleles in the study cohort (94) (Supplemental Table 14). Each peptide was

synthesized and conjugated to a unique oligonucleotide barcode via a UV-cleavable linker to allow antigen-specific cell tagging. Peripheral blood mononuclear cells (PBMCs) from the post-booster cohort were incubated with the pooled peptide–barcode conjugates to enable multimer formation and antigen-specific T cell labeling. $CD8^+$ T cells were enriched using magnetic beads, followed by fluorescence-activated cell sorting (FACS) to isolate barcode-positive antigen-specific T cells. Sorted cells were subjected to single-cell RNA and paired TCR V(D)J sequencing using the 10x Genomics Chromium platform. Library preparation followed the manufacturer's Single Cell Immune Profiling protocol, and sequencing was performed on an Illumina NovaSeq 6000 system. Data were processed with Cell Ranger, and downstream analysis, including transcriptional clustering, TCR repertoire reconstruction, and clonal diversity profiling, was conducted using Seurat and scRepertoire (95). Clonal dominance was defined by proportional representation of TCR clonotypes, and pathway enrichment analysis was performed on transcriptomic profiles of dominant clonotypes to identify exhaustion- and activation-related signatures. Barcode identity confirmed peptide-specificity for each TCR, enabling precise mapping of vaccine-responsive T cell clones.

Drug selection and annotation

Drug–gene interactions were identified using DGIdb v5.0.9 (96). Candidate genes derived from machine learning, network analysis, and trajectory inference were used as input. FDA-approved drugs targeting these genes were retained. Compound annotations, including mechanism of action and pathway specificity, were retrieved from DrugBank (https://www.drugbank.com/clinical/drug_drug_interaction_checker) and ChEMBL (https://www.ebi.ac.uk/chembl/) for further curation.

Transcription factor simulation knockout using CellOracle

To investigate potential regulators of the monocyte transcriptional trajectory, we employed CellOracle (v0.20.0) to simulate transcription factor perturbations in silico (97). Gene regulatory networks (GRNs) were constructed separately for each group using preprocessed single-cell data, with promoter-based TF binding motif information as prior. The GRN construction was performed using the default pipeline with ridge regression for gene–TF interaction inference.

To model the effect of TF perturbation, we conducted in silico knockout (KO) simulations on *FOXO1*, a transcription factor implicated in metabolic and redox regulation. The KO simulation predicts how the absence of *FOXO1* affects downstream gene expression and cellular dynamics, represented as vector fields on the UMAP embedding. Resultant trajectory shifts were visualized using quiver plots, and predicted directionality was compared with observed monocyte differentiation states. Genes with high regulatory weights in the *FOXO1* network were further analyzed to interpret functional consequences of *FOXO1* modulation.

References

64. Li Y, Qin S, Dong L, Qiao S, Wang X, Yu D, et al. Long-term effects of Omicron BA. 2 breakthrough infection on immunity-metabolism balance: a 6-month prospective study. *Nature Communications.* 2024;15(1):2444.
65. Abe K, Abe N, Sugaya T, Takahata Y, Fujita M, Hayashi M, et al. Characteristics of peripheral blood mononuclear cells and potential related molecular mechanisms in patients with autoimmune hepatitis: a single-cell RNA sequencing analysis. *Medical Molecular Morphology.* 2024;57(2):110-23.

66. Lee H, Joo JY, Song JM, Kim HJ, Kim YH, and Park HR. Immunological link between periodontitis and type 2 diabetes deciphered by single-cell RNA analysis. *Clinical and Translational Medicine.* 2023;13(12):e1503.
67. Yang P, Luan M, Li W, Niu M, He Q, Zhao Y, et al. Single-cell transcriptomics reveals peripheral immune responses in non-segmental vitiligo. *Frontiers in Immunology.* 2023;14:1221260.
68. Xu C, Yang J, Kosters A, Babcock BR, Qiu P, and Ghosn EE. Comprehensive multi-omics single-cell data integration reveals greater heterogeneity in the human immune system. *Iscience.* 2022;25(10).
69. Giroux NS, Ding S, McClain MT, Burke TW, Petzold E, Chung HA, et al. Differential chromatin accessibility in peripheral blood mononuclear cells underlies COVID-19 disease severity prior to seroconversion. *Scientific reports.* 2022;12(1):11714.
70. Boukhaled GM, Gadalla R, Elsaesser HJ, Abd-Rabbo D, Quevedo R, Yang SC, et al. Pre-encoded responsiveness to type I interferon in the peripheral immune system defines outcome of PD1 blockade therapy. *Nature immunology.* 2022;23(8):1273-83.
71. Terzoli S, Marzano P, Cazzetta V, Piazza R, Sandrock I, Ravens S, et al. Expansion of memory Vδ2 T cells following SARS-CoV-2 vaccination revealed by temporal single-cell transcriptomics. *npj Vaccines.* 2024;9(1):63.
72. Zheng GXY, Terry JM, Belgrader P, Ryvkin P, Bent ZW, Wilson R, et al. Massively parallel digital transcriptional profiling of single cells. *Nature Communications.* 2017;8(1):14049.
73. Gayoso A, Lopez R, Xing G, Boyeau P, Valiollah Pour Amiri V, Hong J, et al. A Python library for probabilistic analysis of single-cell omics data. *Nature Biotechnology.* 2022;40(2):163-6.
74. Hao Y, Hao S, Andersen-Nissen E, Mauck WM, III, Zheng S, Butler A, et al. Integrated analysis of multimodal single-cell data. *Cell.* 2021;184(13):3573-87.e29.
75. Aran D, Looney AP, Liu L, Wu E, Fong V, Hsu A, et al. Reference-based analysis of lung single-cell sequencing reveals a transitional profibrotic macrophage. *Nature Immunology.* 2019;20(2):163-72.
76. Lindeboom RGH, Worlock KB, Dratva LM, Yoshida M, Scobie D, Wagstaffe HR, et al. Human SARS-CoV-2 challenge uncovers local and systemic response dynamics. *Nature.* 2024;631(8019):189-98.
77. Huse K, Bai B, Hilden VI, Bollum LK, Våtsveen TK, Munthe LA, et al. Mechanism of CD79A and CD79B support for IgM+ B cell fitness through B cell receptor surface expression. *The Journal of Immunology.* 2022;209(10):2042-53.
78. Notarbartolo S, Ranzani V, Bandera A, Gruarin P, Bevilacqua V, Putignano AR, et al. Integrated longitudinal immunophenotypic, transcriptional, and repertoire analyses delineate immune responses in patients with COVID-19. *Science immunology.* 2021;6(62):eabg5021.
79. Villani A-C, Satija R, Reynolds G, Sarkizova S, Shekhar K, Fletcher J, et al. Single-cell RNA-seq reveals new types of human blood dendritic cells, monocytes, and progenitors. *Science.* 2017;356(6335):eaah4573.
80. Zhou L-J, and Tedder TF. Human blood dendritic cells selectively express CD83, a member of the immunoglobulin superfamily. *Journal of immunology (Baltimore, Md: 1950).* 1995;154(8):3821-35.

81. Tracey M, Kevin J, and Cerami PD, Anthony. Tumor necrosis factor: A pleiotropic cytokine and therapuetic target. *Annual review of medicine.* 1994;45(1):491-503.
82. Zawada AM, Rogacev KS, Rotter B, Winter P, Marell R-R, Fliser D, et al. SuperSAGE evidence for CD14++ CD16+ monocytes as a third monocyte subset. *Blood, The Journal of the American Society of Hematology.* 2011;118(12):e50-e61.
83. Förster R, Schubel A, Breitfeld D, Kremmer E, Renner-Müller I, Wolf E, et al. CCR7 coordinates the primary immune response by establishing functional microenvironments in secondary lymphoid organs. *Cell.* 1999;99(1):23-33.
84. Dinarello CA. Biologic basis for interleukin-1 in disease. 1996.
85. Raudvere U, Kolberg L, Kuzmin I, Arak T, Adler P, Peterson H, et al. g:Profiler: a web server for functional enrichment analysis and conversions of gene lists (2019 update). *Nucleic Acids Research.* 2019;47(W1):W191-W8.
86. Wu T, Hu E, Xu S, Chen M, Guo P, Dai Z, et al. clusterProfiler 4.0: A universal enrichment tool for interpreting omics data. *The Innovation.* 2021;2(3).
87. Chen T, and Guestrin C. *Proceedings of the 22nd ACM SIGKDD International Conference on Knowledge Discovery and Data Mining*. San Francisco, California, USA: Association for Computing Machinery; 2016:785–94.
88. Morabito S, Reese F, Rahimzadeh N, Miyoshi E, and Swarup V. hdWGCNA identifies co-expression networks in high-dimensional transcriptomics data. *Cell Reports Methods.* 2023;3(6).
89. Setty M, Kiseliovas V, Levine J, Gayoso A, Mazutis L, and Pe'er D. Characterization of cell fate probabilities in single-cell data with Palantir. *Nature Biotechnology.* 2019;37(4):451-60.
90. Street K, Risso D, Fletcher RB, Das D, Ngai J, Yosef N, et al. Slingshot: cell lineage and pseudotime inference for single-cell transcriptomics. *BMC Genomics.* 2018;19(1):477.
91. Van den Berge K, Roux de Bézieux H, Street K, Saelens W, Cannoodt R, Saeys Y, et al. Trajectory-based differential expression analysis for single-cell sequencing data. *Nature communications.* 2020;11(1):1201.
92. Aibar S, González-Blas CB, Moerman T, Huynh-Thu VA, Imrichova H, Hulselmans G, et al. SCENIC: single-cell regulatory network inference and clustering. *Nature methods.* 2017;14(11):1083-6.
93. Jin S, Guerrero-Juarez CF, Zhang L, Chang I, Ramos R, Kuan C-H, et al. Inference and analysis of cell-cell communication using CellChat. *Nature Communications.* 2021;12(1):1088.
94. Reynisson B, Alvarez B, Paul S, Peters B, and Nielsen M. NetMHCpan-4.1 and NetMHCIIpan-4.0: improved predictions of MHC antigen presentation by concurrent motif deconvolution and integration of MS MHC eluted ligand data. *Nucleic acids research.* 2020;48(W1):W449-W54.
95. Borcherding N, Bormann NL, and Kraus G. scRepertoire: An R-based toolkit for single-cell immune receptor analysis. *F1000Research.* 2020;9:47.
96. Cannon M, Stevenson J, Stahl K, Basu R, Coffman A, Kiwala S, et al. DGIdb 5.0: rebuilding the drug–gene interaction database for precision medicine and drug discovery platforms. *Nucleic acids research.* 2024;52(D1):D1227-D35.
97. Kamimoto K, Stringa B, Hoffmann CM, Jindal K, Solnica-Krezel L, and Morris SA. Dissecting cell identity via network inference and in silico gene perturbation. *Nature.* 2023;614(7949):742-51.

Supplementary Tables

Table 1. Clinical and demographic features of kidney transplant recipients of discovery cohort. Immunosuppressive medication use was assessed at the pre-vaccination baseline.

Variable	Non-responders (n=15)	Responders (n=13)
Age, median (IQR)	65 (56-74)	60 (35-77)
Sex, % male	60%	38%
Time since transplant (years)	15 (4-23)	15 (6-26)
Cyclosporine (CSA) use, n (%)	5, (33%)	6, (46%)
Tacrolimus (FK) use, n (%)	15, (100%)	11, (85%)
mTOR use, n (%)	7, (47%)	3, (23%)
Mycophenolic acid (MPA) use, n (%)	15, (100%)	13, (100%)
Azathioprine (AZA) use, n (%)	1, (7%)	1, (8%)
Methylprednisolone (MP) use, n (%)	12, (80%)	9, (69%)
Prednisolone (P) use, n (%)	14, (93%)	13, (100%)
Rituximab use, n (%)	4, (27%)	0, (0%)
Bortezomib use, n (%)	1, (7%)	0, (0%)
Human Immunoglobulin G (HIG) use, n (%)	2, (13%)	1, (8%)
Anti–SARS-CoV-2 Spike S1 IgG (IU/mL)	< 0.4	993.2 (1.05-5674)

Table 2. Clinical and demographic features of kidney transplant recipients of independent cohort.

Variable	Non-responders (n=5)	Responders (n=12)
Age, median (IQR)	55 (44-72)	54 (37-68)
Sex, % male	40%	42%
Time since transplant (years)	13 (3-19)	16 (6-26)
Cyclosporine (CSA) use, n (%)	2, (40%)	4, (33%)
Tacrolimus (FK) use, n (%)	5, (100%)	10, (83%)
mTOR use, n (%)	2, (40%)	7, (58%)
Mycophenolic acid (MPA) use, n (%)	3, (60%)	7, (58%)
Azathioprine (AZA) use, n (%)	1, (20%)	1, (8%)
Methylprednisolone (MP) use, n (%)	5, (100%)	9, (75%)
Prednisolone (P) use, n (%)	4, (80%)	12, (100%)
Rituximab use, n (%)	2, (40%)	0, (0%)
Bortezomib use, n (%)	1, (20%)	0, (0%)
Human Immunoglobulin G (HIG) use, n (%)	1, (20%)	1, (8%)
Anti–SARS-CoV-2 Spike S1 IgG (IU/mL)	< 0.4	3638 (14.03-15003)

Table 3. Summary of kidney transplant recipient single-cell sample datasets.

Timepoint	Dataset source	Vaccine type	Cohort type	Platform	No. of Samples
Pre-vaccine	In-house	mRNA-1273	Discovery cohort	10X Genomics Chromium	17
Post–1st dose					26
Pre-vaccine		bnt162b2	Independent cohort		7
Post-booster		mRNA-1273			11
		bnt162b2			2
Total					**63**

Table 4. Summary of healthy control single-cell sample datasets.

Dataset source	Publish year	Timepoint	Platform	No. of Samples
In-house	N/A	Pre-vaccine	10X Genomics Chromium	10
GSE240694	2023		Illumina NovaSeq 6000	4
GSE216064	2024		Illumina NovaSeq 6000	4
GSE244515	2023		HiSeq X Ten	11
GSE231794	2023		HiSeq X Ten	3
GSE181543	2022		Illumina NovaSeq 6000	3
GSE206283	2022		Illumina NovaSeq 6000	5
GSE199994	2022		Illumina NovaSeq 6000	2
GSE260763	2024	Post-vaccine	Illumina NovaSeq 6000	28
Total				**70**

Table 5. Chi-squared test results for differences in cell type proportions between groups, with p-values, false discovery rate (FDR)–adjusted values, and significance status.

Cell Type	chi_squared	p_value	fdr	significant
Naive CD4+ T cells	1.30E+01	1.49E-03	1.22E-02	TRUE
Dendritic cells	1.20E+01	2.44E-03	1.22E-02	TRUE
Regulatory T cells	1.19E+01	2.61E-03	1.22E-02	TRUE
Memory CD4+ T cells	1.16E+01	3.04E-03	1.22E-02	TRUE
Non-classical Monocytes	1.03E+01	5.78E-03	1.66E-02	TRUE
B cells	1.00E+01	6.58E-03	1.66E-02	TRUE
Classical Monocytes	9.85E+00	7.26E-03	1.66E-02	TRUE
Helper CD4+ T cells	9.48E+00	8.74E-03	1.75E-02	TRUE
Naive CD8+ T cells	8.13E+00	1.71E-02	3.05E-02	TRUE
Plasmacytoid Dendritic cells	5.39E+00	6.76E-02	1.00E-01	FALSE
Nature killer T cells	5.35E+00	6.89E-02	1.00E-01	FALSE
Nature killer cells	4.07E+00	1.31E-01	1.64E-01	FALSE
Effector memory CD8+ T cells	4.03E+00	1.33E-01	1.64E-01	FALSE
Gamma delta T cells	2.73E+00	2.55E-01	2.82E-01	FALSE
Erythroid cells	2.66E+00	2.64E-01	2.82E-01	FALSE
Megakaryocytes	3.89E-01	8.23E-01	8.23E-01	FALSE

Table 6. Number of cells (n) and relative proportions of each immune cell type in healthy controls, pre-vaccination responder and non-responders.

Condition	Cell Type	n	Proportion
Healthy control	Classical Monocytes	36490	0.207
Healthy control	Naive CD4+ T cells	30661	0.174
Healthy control	Effector memory CD8+ T cells	19856	0.113
Healthy control	Memory CD4+ T cells	20864	0.119
Healthy control	Nature killer cells	18119	0.103
Healthy control	B cells	9035	0.051
Healthy control	Naive CD8+ T cells	10398	0.059
Healthy control	Nature killer T cells	6694	0.038
Healthy control	Helper CD4+ T cells	4129	0.023
Healthy control	Gamma delta T cells	4809	0.027
Healthy control	Non-classical Monocytes	3074	0.017
Healthy control	Megakaryocytes	2390	0.014
Healthy control	Regulatory T cells	6046	0.034
Healthy control	Dendritic cells	1447	0.008
Healthy control	Erythroid cells	1172	0.007
Healthy control	Plasmacytoid Dendritic cells	839	0.005
Pre-vaccination non-responder	Classical Monocytes	25790	0.325
Pre-vaccination non-responder	Naive CD4+ T cells	6408	0.081
Pre-vaccination non-responder	Effector memory CD8+ T cells	11874	0.149
Pre-vaccination non-responder	Memory CD4+ T cells	5201	0.065
Pre-vaccination non-responder	Nature killer cells	10121	0.127
Pre-vaccination non-responder	B cells	2745	0.035
Pre-vaccination non-responder	Naive CD8+ T cells	1472	0.019
Pre-vaccination non-responder	Nature killer T cells	5915	0.074
Pre-vaccination non-responder	Helper CD4+ T cells	1425	0.018
Pre-vaccination non-responder	Gamma delta T cells	674	0.008
Pre-vaccination non-responder	Non-classical Monocytes	3448	0.043
Pre-vaccination non-responder	Megakaryocytes	864	0.011
Pre-vaccination non-responder	Regulatory T cells	1814	0.023
Pre-vaccination non-responder	Dendritic cells	997	0.013
Pre-vaccination non-responder	Erythroid cells	337	0.004
Pre-vaccination non-responder	Plasmacytoid Dendritic cells	341	0.004
Pre-vaccination responder	Classical Monocytes	5695	0.219
Pre-vaccination responder	Naive CD4+ T cells	2901	0.112
Pre-vaccination responder	Effector memory CD8+ T cells	3716	0.143
Pre-vaccination responder	Memory CD4+ T cells	2103	0.081
Pre-vaccination responder	Nature killer cells	3071	0.118
Pre-vaccination responder	B cells	2568	0.099

Pre-vaccination responder	Naive CD8+ T cells	862	0.033
Pre-vaccination responder	Nature killer T cells	1056	0.041
Pre-vaccination responder	Helper CD4+ T cells	824	0.032
Pre-vaccination responder	Gamma delta T cells	633	0.024
Pre-vaccination responder	Non-classical Monocytes	1239	0.048
Pre-vaccination responder	Megakaryocytes	283	0.011
Pre-vaccination responder	Regulatory T cells	558	0.021
Pre-vaccination responder	Dendritic cells	122	0.005
Pre-vaccination responder	Erythroid cells	246	0.009
Pre-vaccination responder	Plasmacytoid Dendritic cells	84	0.003

Table 7. Abundance ratios of monocytes to $CD4^+$ and $CD8^+$ T cells in individual samples.

Sample	Monocyte ratio	CD4 ratio	CD8 ratio	Mono/CD4	Mono/CD8	Condition
3F3322	0.49	0.12	0.02	4.11	26.31	HC
52BA23	0.16	0.27	0.02	0.58	7.20	
655A91	0.16	0.15	0.03	1.11	4.99	
94D44E	0.26	0.13	0.03	2.07	8.19	
HD1_GEX	0.21	0.14	0.03	1.45	6.11	
HD2_GEX	0.24	0.01	0.00	18.57	199.63	
Kolab	0.22	0.06	0.05	3.69	4.33	
P0_S1	0.18	0.14	0.07	1.27	2.49	
P0_S2	0.18	0.12	0.05	1.55	3.40	
P0_S3	0.15	0.12	0.05	1.26	3.06	
P0_S4	0.23	0.21	0.07	1.10	3.35	
P0_S5	0.11	0.15	0.05	0.75	2.28	
P0_S6	0.12	0.18	0.11	0.69	1.07	
PBMC_from_healthy_control_1	0.36	0.20	0.02	1.85	21.56	
S74	0.07	0.13	0.06	0.57	1.20	
S76	0.18	0.27	0.12	0.67	1.51	
S78	0.17	0.18	0.05	0.94	3.16	
S81	0.37	0.09	0.07	4.22	5.30	
healthy_control_1	0.19	0.29	0.06	0.67	3.44	
healthy_control_10	0.02	0.18	0.01	0.13	1.74	
healthy_control_11	0.21	0.28	0.01	0.75	14.78	
healthy_control_2	0.10	0.28	0.12	0.36	0.88	
healthy_control_4	0.02	0.33	0.04	0.06	0.53	
healthy_control_5	0.14	0.23	0.05	0.60	3.07	
healthy_control_7	0.06	0.35	0.09	0.19	0.70	
healthy_control_8	0.20	0.15	0.14	1.38	1.49	
healthy_control_PBMC	0.11	0.43	0.02	0.26	4.88	
V02_ID0	0.28	0.03	0.01	8.45	22.32	Pre-vaccination NR
V16_ID0	0.53	0.06	0.01	9.19	88.95	
V24_ID0	0.40	0.05	0.00	7.90	81.97	
V36_ID0	0.21	0.28	0.05	0.77	4.10	
V47_ID0	0.61	0.09	0.02	7.07	26.88	
V50_ID0	0.12	0.10	0.04	1.27	2.74	
V51_ID0	0.35	0.09	0.02	3.83	18.77	
V54_ID0	0.26	0.08	0.01	3.06	20.41	
V56_ID0	0.32	0.10	0.01	3.13	21.87	
V20_ID0	0.08	0.10	0.03	0.76	2.85	
V23_ID0	0.01	0.05	0.01	0.25	1.48	

V26_ID0	0.17	0.12	0.07	1.48	2.42	Pre-vaccination R
V44_ID0	0.27	0.17	0.04	1.61	6.32	
V45_ID0	0.07	0.08	0.01	0.96	13.50	
V52_ID0	0.34	0.12	0.02	2.86	15.77	
V53_ID0	0.15	0.14	0.02	1.12	8.75	
V57_ID0	0.14	0.15	0.13	0.96	1.09	

Table 8. Linear regression AUC values for baseline and metabolism-integrated models, with ΔAUC and statistical significance for each immune cell type.

Cell Type	auc_baseline	auc_with_metabolism	delta_auc	p_value	n_cells
Classical Monocytes	0.67	0.77	0.09	4.13E-165	31485
B cells	0.66	0.76	0.1	1.27E-48	5313
Naive CD4+ T cells	0.59	0.67	0.09	5.02E-41	9309
Effector memory CD8+ T cells	0.61	0.67	0.06	4.19E-34	15590
Non-classical Monocytes	0.78	0.84	0.06	2.88E-28	4687
Nature killer cells	0.62	0.67	0.05	4.23E-27	13192
Memory CD4+ T cells	0.59	0.66	0.08	2.42E-26	7304
Helper CD4+ T cells	0.58	0.7	0.12	7.86E-19	2249
Dendritic cells	0.62	0.86	0.23	7.62E-15	1119
Naive CD8+ T cells	0.62	0.7	0.08	5.80E-14	2334
Regulatory T cells	0.59	0.68	0.09	1.18E-10	2372
Erythroid cells	0.66	0.78	0.12	2.75E-08	583
Plasmacytoid Dendritic cells	0.72	0.87	0.16	8.23E-08	425
Gamma delta T cells	0.69	0.74	0.05	4.87E-07	1307
Megakaryocytes	0.6	0.66	0.06	0.00175303	1147

Table 9. Top 30 differentially expressed genes (DEG) in classical monocytes comparing non-responders and responders at the pre-vaccination timepoint.

Genes	p_val	avg_log2FC	pct.1	pct.2	p_val_adj
MT-ATP8	0	1.049	0.851	0.677	0.00E+00
HLA-DRB5	7.75E-275	0.927	0.56	0.288	4.46E-270
MT-CO3	0	0.799	0.989	0.947	0.00E+00
FOLR3	4.09E-60	0.788	0.244	0.144	2.36E-55
MT-CO2	0	0.771	0.995	0.981	0.00E+00
MT-CO1	0	0.691	0.996	0.985	0.00E+00
MT-CYB	0	0.677	0.927	0.811	0.00E+00
MT-ND4	0	0.674	0.969	0.901	0.00E+00
HFM1	7.85E-84	0.654	0.227	0.1	4.52E-79
MT-ND3	0	0.644	0.982	0.957	0.00E+00
SOCS3	7.40E-71	0.631	0.318	0.197	4.26E-66
CRIP1	9.85E-49	0.562	0.835	0.82	5.68E-44
HLA-DQA1	3.10E-125	0.551	0.227	0.069	1.78E-120
MT-ND2	3.17E-277	0.548	0.949	0.889	1.82E-272
MT-ND1	0	0.544	0.981	0.953	0.00E+00
NEAT1	1.13E-248	0.515	0.983	0.969	6.52E-244
ACSL1	8.14E-46	0.514	0.642	0.568	4.69E-41
MT-ATP6	0	0.513	0.959	0.894	0.00E+00
MT-ND4L	1.50E-131	0.512	0.743	0.597	8.65E-127
LGALS1	7.62E-300	0.506	0.977	0.942	4.39E-295
HIF1A	3.25E-108	0.505	0.735	0.631	1.87E-103
NRG1	8.11E-102	0.497	0.329	0.167	4.67E-97
XIST	4.33E-143	0.492	0.228	0.057	2.50E-138
PCBP1	6.20E-196	0.49	0.805	0.649	3.57E-191
PLCB1	1.52E-87	0.47	0.555	0.405	8.76E-83
MYO1F	1.62E-189	0.458	0.914	0.858	9.35E-185
MT-ND5	8.82E-139	0.458	0.79	0.66	5.08E-134
PCBP2	3.80E-114	0.447	0.713	0.572	2.19E-109
ADGRE2	1.41E-89	0.447	0.503	0.343	8.10E-85
RPS4X	1.43E-216	0.444	0.979	0.956	8.23E-212

Table 10. Top enriched Gene Ontology biological pathways of classical monocytes from pre-vaccination non-responders versus responders.

Condition	significant	p_value	term_size	query_size	intersection_size	precision	recall	term_id	source	term_name
Pre-vaccine R	TRUE	4.75E-32	1809	270	96	0.355556	0.053068	GO:0006952	GO:BP	defense response
	TRUE	4.43E-30	1593	270	88	0.325926	0.055242	GO:0009607	GO:BP	response to biotic stimulus
	TRUE	8.36E-30	1724	270	91	0.337037	0.052784	GO:0044419	GO:BP	biological process involved in interspecies interaction between organisms
	TRUE	2.80E-29	1555	270	86	0.318519	0.055305	GO:0051707	GO:BP	response to other organism
	TRUE	3.22E-29	1558	270	86	0.318519	0.055199	GO:0043207	GO:BP	response to external biotic stimulus
Pre-vaccine NR	TRUE	0.000128	92	229	10	0.043668	0.108696	GO:0019646	GO:BP	aerobic electron transport chain
	TRUE	0.000133	145	229	12	0.052402	0.082759	GO:0006119	GO:BP	oxidative phosphorylation
	TRUE	0.000136	5	229	4	0.017467	0.8	GO:0015988	GO:BP	energy coupled proton transmembrane transport, against electrochemical gradient
	TRUE	0.000136	5	229	4	0.017467	0.8	GO:0015990	GO:BP	electron transport coupled proton transport
	TRUE	0.00016	618	229	24	0.104803	0.038835	GO:1901699	GO:BP	cellular response to nitrogen compound

Table 11. Relative abundance of classical monocyte subclusters across three conditions.

Condition	Leiden_0	Leiden_1	Leiden_2	Leiden_3	Leiden_4	Leiden_5
Healthy control	21%	31.20%	23.90%	10.10%	12.60%	1.15%
Pre-vaccination non-responder	29.30%	25.80%	21.10%	13%	9.19%	1.64%
Pre-vaccination responder	31.10%	22.70%	27.10%	11.80%	5.39%	1.93%

Table 12. Top 30 differentially expressed genes (DEG) in classical monocytes cluster 4 comparing non-responders and responders at the pre-vaccination timepoint.

Genes	p_val	avg_log2FC	pct.1	pct.2	p_val_adj
FOLR3	7.62E-10	1.205	0.271	0.09	4.39E-05
MINOS1	1.81E-27	1.114	0.479	0.073	1.04E-22
SEPT9	2.10E-20	1.009	0.344	0.038	1.21E-15
C8orf59	1.67E-21	1.003	0.379	0.051	9.60E-17
FAM96B	5.98E-19	0.970	0.316	0.03	3.45E-14
PCBP2	4.41E-26	0.963	0.75	0.41	2.54E-21
MT-CO2	6.04E-43	0.921	0.979	0.906	3.48E-38
MT-CO3	1.81E-33	0.827	0.958	0.803	1.04E-28
RARRES3	8.89E-16	0.822	0.256	0.017	5.12E-11
CD99	9.08E-16	0.770	0.715	0.423	5.23E-11
FAM96A	1.79E-16	0.770	0.304	0.038	1.03E-11
C19orf70	1.03E-14	0.749	0.285	0.043	5.92E-10
ALDOA	1.04E-20	0.726	0.858	0.594	5.97E-16
EEF1A1	1.41E-35	0.656	0.991	0.987	8.11E-31
RGS10	5.78E-14	0.656	0.509	0.218	3.33E-09
C19orf24	1.11E-13	0.644	0.243	0.026	6.42E-09
RPL6	5.12E-30	0.632	0.969	0.893	2.95E-25
HLA-DRB1	6.83E-09	0.628	0.814	0.697	0.000394
MIDN	1.96E-11	0.627	0.391	0.15	1.13E-06
SOCS3	2.31E-07	0.626	0.265	0.107	0.013335
RPS10	3.89E-14	0.625	0.564	0.278	2.24E-09
RPS20	5.30E-13	0.602	0.602	0.329	3.05E-08
NCBP2-AS2	8.61E-11	0.601	0.171	0.009	4.96E-06
PIM1	5.47E-09	0.594	0.207	0.047	0.000315
LGALS1	7.13E-18	0.581	0.924	0.786	4.11E-13
AES	1.06E-09	0.568	0.215	0.043	6.12E-05
FIS1	3.63E-10	0.563	0.454	0.214	2.09E-05
S100A10	3.48E-15	0.562	0.961	0.859	2.00E-10
GAPDH	3.65E-20	0.556	0.976	0.932	2.11E-15

Table 13. Co-expression module genes of NR-M2 and NR-M3.

NR-M2	NR-M3
CD99	POLDIP2
ARF5	POLR2J
NDUFAB1	GGCT
SLC25A5	CDK11A
REX1BD	SS18L2
CCDC124	RPS20
PSMB1	UQCRC1
TYROBP	CD4
HEBP1	PTBP1
VIM	TMEM159
TMSB10	PSMC4
GABARAPL2	SLC25A39
CAPG	MDH1
AP2S1	MARCO
MRPL43	CD74
MRPS24	RNH1
RPL18	STRAP
CTSA	RNASET2
PABPC1	GRN
MGAT4A	PSMA4
SRI	HSPA5
ACTB	UTS2
GSTP1	HERPUD1
FCN1	PHPT1
MGST2	SEC61A1
FTL	SNRNP40
PSMC5	ACAA1
RTRAF	EIF4B
FKBP1A	U2AF2

Table 14. Peptide sequences used for BEAM-T antigen specificity profiling.

Peptide sequence
KWPWYIWLGF
QYIKWPWYIW
LYNSASFSTF
FLPFFSNVTW
SFKEELDKYF
VGYQPYRVVV

Table 15. Drug-gene interaction results of candidate drugs.

Gene	Drug	Regulatory approval	Indication	Interaction Score
RAC1	CHEMBL:CHEMBL554475	Not Approved	N/A	5.800422062
RAC1	AZATHIOPRINE	Approved	N/A	0.305285372
RAC1	CHEMBL:CHEMBL563777	Not Approved	N/A	5.800422062
RAC1	CHEMBL:CHEMBL562095	Not Approved	N/A	5.800422062
RAC1	CHEMBL:CHEMBL579882	Not Approved	N/A	5.800422062
RAC1	VEMURAFENIB	Approved	antineoplastic agent	0.156768164
RAC1	DABRAFENIB	Approved	antineoplastic agent	0.214830447
RAC1	PLX-4720	Not Approved	N/A	0.64449134
RAC1	NSC 23766	Not Approved	N/A	11.600844112
GAPDH	COMPOUND 5A [PMID: 31287314]	Not Approved	N/A	0.334639734
GAPDH	TOPIRAMATE	Approved	Anticonvulsants; anti-migraine agents,antimigraine agent,anticonvulsant	0.030421794
GAPDH	SLC-0111	Not Approved	N/A	0.669279469
GAPDH	EPINEPHRINE	Approved	anestethic	0.033463973
GAPDH	THIRAM	Not Approved	N/A	0.058198215
GAPDH	BENZOLAMIDE	Not Approved	N/A	1.338558937
GAPDH	CHEMBL:CHEMBL601757	Not Approved	N/A	0.055773289
GAPDH	ACETAZOLAMIDE	Approved	Anticonvulsants; Diuretics; antiglaucomic agent	0.095611353
GAPDH	TAMOXIFEN	Approved	Hormonal,Antineoplastic Agents	0.041186429
GAPDH	COMPOUND 5B [PMID: 31287314]	Not Approved	N/A	0.334639734
GAPDH	CHEMBL:CHEMBL580421	Not Approved	N/A	0.121687176
GAPDH	HISTAMINE	Approved	cytorprotective agent during cancer treatment	0.102966072
GAPDH	SODIUM BUTYRATE	Not Approved	N/A	0.191222705

GAPDH	CHEMBL:CHEMBL139935	Not Approved	N/A	0.121687176
GAPDH	ETHOXZOLAMIDE	Approved	Diuretics; Antiglaucoma agents,Antihypertensive Agents	0.089237262
GAPDH	ANESTHETIC AGENT	Not Approved	N/A	0.267711787
GAPDH	9,10-PHENANTHRENEQUINONE	Not Approved	N/A	0.051483036
GAPDH	CHLORTHALIDONE	Approved	Antihypertensive Agents; Diuretics	0.148728771
GAPDH	ZONISAMIDE	Approved	anticonvulsant,antipsychotic agent,appetite suppressant	0.053542357
GAPDH	SELENIUM	Approved	N/A	0.157477522
GAPDH	INDISULAM	Not Approved	N/A	0.669279469
GAPDH	GALLIC ACID	Not Approved	N/A	1.338558937
GAPDH	METHOCARBAMOL	Approved	N/A	0.223093156
GAPDH	METHAZOLAMIDE	Approved	Diuretics; Antiglaucoma agents,Antihypertensive Agents	0.133855894
GAPDH	ESTRADIOL VALERATE	Approved	for treatment of menopausal symptoms,contraceptive,treatment for menopause,hormone replacement	0.056959955
GAPDH	OMIGAPIL	Not Approved	for treatment of amyotrophic lateral sclerosis (ALS),antiparkinson agent	1.338558937
GAPDH	GALLIC ACID	Not Approved	N/A	0.111546578
GAPDH	DICHLORPHENAMIDE	Approved	Antiglaucomic Agents	0.267711787
GAPDH	SULPIRIDE	Approved	Second-Generation; Antipsychotic Agents,Antidepressive Agents	0.095611353
GAPDH	DEFEROXAMINE	Approved	N/A	0.157477522
GAPDH	HISTIDINE	Approved	N/A	0.167319867
GAPDH	CHEMBL:CHEMBL502775	Not Approved	N/A	0.669279469
GAPDH	DORZOLAMIDE	Approved	N/A	0.267711787
GAPDH	PROTEIN SYNTHESIS INHIBITOR	Not Approved	N/A	0.223093156
GAPDH	PURPUROGALLIN	Not Approved	N/A	0.037182193

GAPDH	BRINZOLAMIDE	Approved	Antiglaucomic Agents	0.33463973 4
GAPDH	CHEMBL:CHEMBL578512	Not Approved	N/A	0.04615720 5
GAPDH	CHEMBL:CHEMBL505670	Not Approved	N/A	0.03824454 1
GAPDH	CHEMBL:CHEMBL429095	Not Approved	N/A	0.02677117 9
MT-ND3	METFORMIN HYDROCHLORIDE	Approved	N/A	0.23305267 2
MT-ND3	ME-344	Not Approved	N/A	0.25590097 3
MT-ND3	NADH	Not Approved	N/A	13.0509496 4
MT-ND3	NV-128	Not Approved	N/A	0.26101899 3
MT-CO2	CELECOXIB	Approved	NSAID	1.55832234 5

Table 16. Donor-level and pseudobulk validation of NR-associated monocyte features. Single-cell measurements were summarized to one value per donor, and pseudobulk profiles were generated by aggregating raw classical-monocyte counts within each donor.

	feature	mean_NR	mean_R	median_NR	median_R	delta_mean_NR_minus_R	cliff_delta_NR_vs_R	direction	p_adj_BH
donor-level score	NR_signature	9.75E-01	2.11E-01	1.10E+00	1.37E-01	7.64E-01	7.78E-01	NR higher	3.26E-02
	MT-ND3	2.86E+00	2.37E+00	2.85E+00	2.40E+00	4.93E-01	7.78E-01	NR higher	3.26E-02
	CD274	3.57E-03	9.49E-04	2.08E-03	0.00E+00	2.62E-03	5.83E-01	NR higher	1.09E-01
	OXPHOS	4.28E-01	3.90E-01	4.19E-01	3.63E-01	3.82E-02	5.56E-01	NR higher	1.21E-01
	MHCII_gene	2.04E-01	-2.30E-01	7.60E-01	-4.19E-01	4.34E-01	3.61E-01	NR higher	3.66E-01
	MHCI	8.06E-01	8.18E-01	7.69E-01	8.04E-01	-1.19E-02	-2.50E-01	R higher	5.51E-01
	MHCII	5.11E-01	4.93E-01	6.04E-01	4.89E-01	1.87E-02	1.94E-01	NR higher	6.08E-01
	Costimulation	7.16E-02	-8.05E-02	1.27E-01	-1.40E-01	1.52E-01	1.39E-01	NR higher	6.65E-01
pseudobulk	OXPHOS	3.55E-01	-3.99E-01	4.65E-01	-4.19E-01	7.54E-01	6.11E-01	NR higher	7.71E-02
	MT-ND3	1.10E+01	1.03E+01	1.11E+01	1.03E+01	6.95E-01	7.22E-01	NR higher	5.66E-02
	MHCII	2.40E-01	-2.70E-01	5.17E-01	-5.68E-01	5.09E-01	3.06E-01	NR higher	3.12E-01
	Costimulation	2.03E-01	-2.28E-01	4.55E-01	-2.14E-01	4.31E-01	4.44E-01	NR higher	1.81E-01

Table 17. Donor-level recorded immunosuppressive medication exposures. Available medication records are shown for each KTR donor by response group. Values indicate recorded exposure or dose information available from the clinical record.

Sample id	Group	Sex	Ab titer (BAU/ml)	Cyclosporine (CSA) (mg)	Tacrolimus (FK) (mg)	mTOR (mg)	Mycophenolic acid_cc (mg)	Mycophenolic acid_mf (mg)	Azathioprine (mg)	Antithymocyte globulin (mg)	Methylprednisolone (mg)	Prednisolone (mg)	Rituximab (mg)	Bortezomib (mg)
V02_ID0	NR	M	< 0.4	0	3.005	0	515	0	0	0	0	10.2	0	0
V16_ID0	NR	F	< 0.4	0	7.64	0	0	228.6	0	0	410.71	10.28	0	0
V20_ID0	R	F	21.51	0	4.61	0	0	205.2	0	0	0	5.55	0	0
V23_ID0	R	F	1947	160.25	0	0	312.5	0	0	0	0	4.57	0	0
V24_ID0	NR	M	< 0.4	175.25	9.86	0	750	0	100	0	343.75	6.19	0	0
V26_ID0	R	F	19.42	172.5	0	0.25	472.5	0	0	0	500	5.06	0	0
V36_ID0	NR	M	< 0.4	0	15.42	0	722.5	540	0	0	369.57	11.07	200	0
V44_ID0	R	M	4.35	0	10.26	0	505	0	0	0	20.12	7.75	0	0
V45_ID0	R	F	32.07	0	14.31	0	280	360	0	0	0	10.95	0	0
V47_ID0	NR	M	< 0.4	0	7	0	562.5	0	0	0	420.45	10.85	500	0
V50_ID0	NR	F	< 0.4	166.25	2.6	1.57	307.5	0	0	0	397.06	15.69	0	0
V51_ID0	NR	F	< 0.4	213.5	5	2.335	467.5	185.4	0	0	500	10.48	500	0
V52_ID0	R	M	16.54	148.25	6.71	0	0	601.2	0	0	300	12.06	0	0
V53_ID0	R	M	1.05	0	1.57	0	0	387	0	0	14.72	5.43	0	0
V54_ID0	NR	F	< 0.4	133	2.4	1.75	535	630	0	0	0	12.26	0	0
V56_ID0	NR	M	< 0.4	0	10.17	1.13	480	720	0	0	343.75	10.43	0	0
V57_ID0	R	F	5674	77.75	12.66	0	332.5	0	0	0	0	9.01	0	0

Table 18. Public healthy-control datasets used for contextual reference analysis.

GEO accession	Healthy-control samples ID	Vaccination context / sampling point	PBMC isolation and handling reported in GEO	Single-cell library / modality	Sequencing platform	Role in this study
GSE240694	S74, S76, S78, S81	Vaccination status not specified in GEO	Original PBMC isolation method not specified. PBMCs were cryopreserved immediately after isolation, thawed into RPMI 1640 with 0.04% BSA, and subjected to dead-cell removal when required.	10x Genomics Chromium Next GEM Single Cell 5′	Illumina NovaSeq 6000	Baseline healthy-reference dataset
GSE231794	PBMC from healthy control 1–3	Vaccination status not specified in GEO	Peripheral blood collected in EDTA tubes was diluted with PBS and layered onto Ficoll-Paque; the PBMC fraction was isolated by density-gradient centrifugation and washed twice with PBS.	Singleron GEXSCOPE single-cell RNA-seq	Illumina HiSeq X Ten	Baseline healthy-reference dataset
GSE244515	healthy control 1–11	Vaccination status not specified in GEO	PBMCs were separated using SepMate tubes with density-gradient medium within 30 minutes of blood collection; diluted blood was centrifuged and the upper layer was collected and washed twice with PBS containing 2% FBS.	10x Genomics Chromium Next GEM Single Cell 3′ v3.1	Illumina HiSeq X Ten	Baseline healthy-reference dataset
GSE216064	healthy control PBMC	Vaccination status not specified in GEO	Peripheral blood was collected into EDTA-2Na tubes and centrifuged to separate PBMCs, which were frozen. Samples were thawed together and filtered through a 40-μm cell strainer before library preparation.	10x Genomics Chromium Single Cell 3′	Illumina NovaSeq 6000	Baseline healthy-reference dataset
GSE181543	PBMC1–3 [GEX]	Vaccination status not specified in GEO	PBMCs were isolated directly from whole blood using the EasySep Direct Human PBMC Isolation Kit.	10x Genomics Single Cell 5′ with Feature Barcoding	Illumina NovaSeq 6000	Baseline healthy-reference dataset

GSE206283	E0FA1E, 3F3322, 94D44E, 52BA23, 655A91	Vaccination status not specified in GEO	Original PBMC isolation method not specified. Frozen PBMCs were thawed, assessed for viability, resuspended in PBS containing 0.04% BSA and RNase inhibitor, and processed for single-cell RNA-seq.	10x Genomics Single Cell 5′ v1	Illumina NovaSeq 6000	Baseline healthy-reference dataset
GSE199994	HD1_GEX, HD2_GEX	Vaccination status not specified in GEO	Original PBMC isolation method not specified. Cryopreserved PBMCs were thawed, treated with DNase, washed, and processed according to the 10x Genomics Multiome workflow.	10x Genomics Single Cell Multiome ATAC + Gene Expression	Illumina NovaSeq 6000	Baseline healthy-reference dataset
GSE260763	VCOV_s01–s06 at P0, P1, and P2	BNT162b2; P0: 1 day before dose 1; P1: 3 days after dose 1; P2: 17 days after dose 1	PBMCs were isolated from buffy coats using Lympholyte-H density-gradient separation. Samples used for single-cell analysis had been cryopreserved in FBS with 10% DMSO and were ≥95% viable after thawing.	10x Genomics Single Cell 5′ paired with γδ TCR-seq	Illumina NovaSeq 6000	Vaccinated healthy-reference dataset for pre-/post-vaccination comparisons